The Astrophysical Journal, 912:160 (25pp), 2021 May 10 https://doi.org/10.3847/1538-4357/abedaa

Tully–Fisher Distances and Dynamical Mass Constraints for 24 Host Galaxies of Reverberation-mapped AGNs

Justin H. Robinson[1], Misty C. Bentz[1], Hélène M. Courtois[2], Megan C. Johnson[3], D. M. Crenshaw[1], Beena Meena[1], Garrett E. Polack[1], Michele L. Silverstein[4,5,6], and Dading Chen[1]

[1] Department of Physics and Astronomy, Georgia State University, Atlanta, GA 30303, USA; jrob@astro.gsu.edu
[2] University of Lyon; UCB Lyon 1/CNRS/IN2P3; IP2I Lyon, France
[3] United States Naval Observatory (USNO) 3450 Massachusetts Avenue NW, Washington, DC 20392, USA
[4] NASA Goddard Space Flight Center, Greenbelt, MD 20771, USA
[5] RECONS Institute, Chambersburg, PA 17201, USA

Received 2020 December 23; revised 2021 March 9; accepted 2021 March 9; published 2021 May 17

Abstract

We present Tully–Fisher distances for 24 active galactic nucleus (AGN) host galaxies with black hole mass ($M_{\rm BH}$) measurements from reverberation mapping, as well as the first calibration of the *V*-band Tully–Fisher relation. Combining our measurements of H I 21 cm emission with Hubble Space Telescope and ground-based optical and near-infrared images allows multiple distance measurements for 19 galaxies and single measurements for the remaining 5. Separation of the nucleus from its host galaxy via surface brightness decomposition yields galaxy-only luminosities, thus allowing measurements of the distance moduli free of contamination from the AGNs. For 14 AGN hosts, these are the first reported distances independent of redshift, and hence independent of peculiar velocities. For the remaining galaxies, we show good agreement between our distances and those previously reported from surface brightness fluctuations and Cepheids. We also determine the total galaxy mass enclosed within the estimated H I radius, which when compared to the baryonic content allows for constraints on the dark matter masses. We find a typical mass fraction of $M_{\rm DM}/M_{\rm DYN} = 62\%$, and find significant correlations between $M_{\rm BH}$–$M_{\rm DYN}$ and $M_{\rm BH}$–$M_{\rm DM}$. Finally, we scale our galaxy radii based on estimated relationships between visible and halo radii and assume a flat rotation curve out to the halo radius to approximate $M_{\rm HALO}$. Over the range of $M_{\rm BH}$ and $M_{\rm HALO}$ in this sample, we find good agreement with observationally constrained relationships between $M_{\rm BH}$ and $M_{\rm HALO}$ and with hydrodynamical simulations.

Unified Astronomy Thesaurus concepts: AGN host galaxies (2017); Galaxy distances (590); Seyfert galaxies (1447); Galaxy masses (607)

1. Introduction

It has become apparent in the past two decades that supermassive black holes (SMBHs) and their host galaxies have a symbiotic relationship (see reviews by Kormendy & Ho 2013 and Heckman & Best 2014), the discovery of which was unexpected given the vast difference in spatial and dynamical scales. The first indication of this was through empirical scaling relationships, for example, the black hole mass–bulge velocity dispersion relation ($M_{\rm BH}-\sigma_\star$; Ferrarese & Merritt 2000; Gebhardt et al. 2000; Kormendy & Ho 2013) and the black hole mass–bulge luminosity relation ($M_{\rm BH}-L_{\rm BULGE}$; Kormendy & Richstone 1995; Kormendy & Ho 2013). To further understand and explore black hole-galaxy evolution, these scaling relations also provide observational evidence to constrain the parameters of large cosmological simulations of galaxy and SMBH growth (Steinborn et al. 2015; Volonteri et al. 2016; Mutlu-Pakdil et al. 2018). The generally accepted interpretation of these scaling relations and simulations is that black hole-galaxy growth is regulated by active galactic nucleus (AGN) feedback (Silk & Rees 1998; Bower et al. 2006; Ciotti et al. 2009; Fanidakis et al. 2011), and thus SMBHs play an important role in galaxy evolution. It is therefore vital to obtain accurate measurements of both galaxy and black hole characteristics for investigating these relationships.

AGN activity not only affects galaxy evolution, it also provides a mechanism for directly constraining the mass of the central black hole through reverberation mapping (RM; Blandford & McKee 1982; Peterson 1993). Variability of the continuum emission is echoed through the variation in flux from the broad emission line region (BLR) gas. The time delay between the continuum signal and the BLR echo provides a measurement of the BLR radius ($R_{\rm BLR}$), which when combined with the velocity of the BLR gas yields a constraint on the enclosed mass, or $M_{\rm BH}$. In effect, RM relies on temporal resolution, as opposed to spatial resolution. Most other techniques that directly constrain $M_{\rm BH}$, such as dynamical modeling, rely on spatial resolution and therefore cannot be applied beyond ~100 Mpc (Gültekin et al. 2009).

While RM measurements are effectively distance independent, they are both time consuming and resource intensive. However, the discovery of the relationship between $R_{\rm BLR}$ and the luminosity of the AGN ($R_{\rm BLR}$–$L_{\rm AGN}$; Koratkar & Gaskell 1991; Kaspi et al. 2000), calibrated with the RM method, has led to an important shortcut for estimating SMBH masses at any redshift (Vestergaard & Peterson 2006; Jiang et al. 2007; Kurk et al. 2007, 2009; Willott et al. 2010). A single spectrum allows a measurement of $L_{\rm AGN}$ to predict $R_{\rm BLR}$, thus allowing $M_{\rm BH}$ to be estimated without investing months or years of spectroscopic monitoring.

The largest known uncertainty in the $R_{\rm BLR}$–$L_{\rm AGN}$ relation is the lack of accurate distances for AGN hosts, which produces uncertainties in the derived luminosities upwards of a factor of

---

[6] NASA Postdoctoral Program Fellow.

$\sim$3 (Bentz et al. 2013). Only nine galaxies in the complete sample of RM AGN systems have distances independent of redshift. Since the sample is dominated by active galactic nuclei (AGNs) with $z \lesssim 0.1$, the majority of distances estimated from redshift may be heavily affected by the velocity field from local gravitational interaction, rather than dominated by Hubble flow. These peculiar velocities ($V_{\rm PEC}$) have been observed to be upwards of 500 km s^{-1} in the local universe (Tully et al. 2008, 2013), which causes significant uncertainty in distances derived solely from spectroscopic redshift. Measurements of galaxy properties that directly depend on distance (e.g., luminosity) and are relied on for SMBH-galaxy scaling relationships are thus hindered by z-based distances. The reverberation sample serves as the basis for all secondary $M_{\rm BH}$ estimates in distant AGNs, so accurate distance determinations are crucial for a large number of RM AGN hosts.

Accurate distance measurements to galaxies in the local universe have allowed tight construction of what is commonly referred to as the cosmic distance ladder. The methods that set the scale for nearly all extragalactic rungs of the ladder are Leavitt's law (Cepheid period–luminosity relationship; Leavitt & Pickering 1912) and the tip of the red giant branch (TRGB; Iben & Renzini 1983; Salaris & Cassisi 1997). Both of these methods require individual stars to be resolved, demanding high resolving power only achievable by a few instruments, thus limiting their reach to $\sim$40 Mpc (Riess et al. 2016). The surface brightness fluctuation (SBF; Tonry et al. 2001; Blakeslee et al. 2010) and Fundamental Plane (Faber & Jackson 1976; Djorgovski & Davis 1987; Dressler et al. 1987) methods are only applicable to early-type galaxies, but most of the optically bright AGNs in the local universe are hosted by spirals.

One of the most widely utilized distance methods for disk galaxies is the Tully–Fisher (TF) relation (Tully & Fisher 1977). The TF relation is an empirical correlation between the rotational velocity of a late-type galaxy and its brightness. A galaxy's mass is constrained by its rotation rate, and its luminosity traces the mass. Therefore, measurement of the maximum rotation rate yields the absolute magnitude of the galaxy, and the difference between the absolute and apparent magnitudes constrains the distance. 21 cm emission from neutral hydrogen (H I), due to its overwhelming abundance in late-type galaxies and extension far past the stellar disk, is usually used to trace disk velocity. Resolved H I surveys (e.g., Walter et al. 2008; Ott et al. 2012; Koribalski et al. 2018; Adams & van Leeuwen 2019; Koribalski et al. 2020; Maddox et al. 2021) provide the most precise method for constraining the maximum rotation rate ($V_{\rm mx}$) through rotation curve analysis. For large samples of galaxies, the rotational broadening of unresolved, integrated H I emission may be used as a proxy for a rotation curve (Epstein 1964; Roberts 1969). The TF relation has traditionally been limited to $z \lesssim 0.1$ (Tully et al. 2008, 2013), even though H I has increasingly been detected at higher redshift (Jaffé et al. 2013; Catinella & Cortese 2015; Fernández et al. 2016). Galaxies with $z \gtrsim 0.1$ are generally assumed to be within the Hubble flow.

We thus undertook a program to measure TF distances for as many RM AGN hosts as possible. In this paper, we use the H I emission lines from Robinson et al. (2019; hereafter Paper I) and present TF distance determinations for 24 Seyfert 1 galaxies. In Section 2, we briefly discuss the H I spectral observations (see Paper I) and describe the imaging of our sample. In Section 3, we describe the two-dimensional surface brightness modeling and separation of the central AGN from the host galaxy in the images. In Section 4, we describe the measurement methods for the calibrated galaxy magnitudes and H I 21 cm line widths. In Section 5, we detail our distance calculations and present the first calibration of the TF relation for the Johnson V band. In Section 6, we report derived values of galaxy dynamical mass ($M_{\rm DYN}$) and dark matter mass ($M_{\rm DM}$) within the H I radius. Finally, in Section 7, we explore the relationships between $M_{\rm DYN}$ and $M_{\rm DM}$ with $M_{\rm BH}$.

Throughout this work we adopt a Lambda cold dark matter cosmology (ΛCDM) of $\rm H_0 = 74$ km s^{-1} Mpc^{-1} (Riess et al. 2019), $\Omega_{\rm M} = 0.27$, and $\Omega_\Lambda = 0.73$ (Bennett et al. 2014).

2. Spectroscopy and Imaging

In Paper I, we presented H I spectroscopy of 31 AGN hosts with direct $M_{\rm BH}$ measurements from the RM database of Bentz & Katz (2015), and constraints on gas mass ($M_{\rm GAS}$) and total baryonic mass ($M_{\rm BARY}$). Here, we briefly summarize the 21 cm observations and describe the optical and near-infrared imaging of the AGN hosts.

2.1. *H I 21 cm Spectra*

Spectroscopy of the H I 21 cm emission lines was acquired in 2013 (GBT13A-468; PI: Ou-Yang) and 2018/2019 (GBT18B-258; PI: Robinson) with the Robert C. Byrd Green Bank Telescope[7] (GBT). The observational setups and instrument selections are detailed in Paper I. In brief, both data sets were observed in position-switched mode with equal on–off exposure pairs and typical exposures of 60 s scans for GBT13A-468 and 120 s scans for GBT18B-258. All scans were broken into 3 s integrations to aid in radio frequency interference removal.

Spectral reduction was carried out with the GBTIDL suite (Marganian et al. 2006) v2.8 for GBT13A-468 and v2.10.1 for GBT18B-258. Each on–off pair was combined with the standard (ON–OFF)/OFF procedure, and all exposures for one source were accumulated and averaged into a single spectrum. Low-order polynomials were fit to and subtracted from the baselines before spectral measurements were conducted.

While we detected H I emission lines from 31 of the 44 AGN host galaxies that were observed, we limit the analysis here to the 24 galaxies that exhibit a rotationally broadened dual-horned profile shape, as this is needed to recover the disk velocity information for use in TF distance determinations. Additionally, we note that although we limit this sample to dual-horned profiles, the galaxy inclinations tend to be oriented more face-on (<45°) than the typical galaxies targeted for TF-based distances. The 24 galaxies are listed in Table 1.

2.2. *Optical and Near-infrared Imaging*

Optical and near-infrared images of the AGN host galaxies have been compiled from several observatories, with the goal of separating the AGN contribution from the galaxy via two-dimensional surface brightness decomposition (described in

---

[7] The Green Bank Observatory is a facility of the National Science Foundation operated under cooperative agreement by Associated Universities, Inc.

Table 1
Optical and Near-IR Imaging

Target	R.A. (hh mm ss.s)	Decl. (dd mm ss)	z	Date (yyyy-mm-dd)	Exp Time (s)	Obs. Setup
Mrk 1044	02 30 05.5	−08 59 53	0.01645	2011 Jan 10	725.0	HST WFC3 F547M
				2019 Dec 20	810.0	APO 3.5 m ARCTIC B
				2019 Dec 20	240.0	APO 3.5 m ARCTIC V
				2019 Sep 28	90.0	APO 3.5 m ARCTIC R
				2019 Sep 28	60.0	APO 3.5 m ARCTIC I
Ark 120	05 16 11.4	−00 08 66	0.03271	2006 Oct 30	2040.0	HST ACS HRC F550M
MCG+08-11-011	05 54 53.6	+46 26 22	0.02048	2016 May 21	2370.0	HST WFC3 F547M
Mrk 6	06 52 12.2	+74 25 37	0.01881	2014 Nov 06	2620.0	HST WFC3 F547M
				2020 Feb 12	60.0	APO 3.5 m ARCTIC V
				2012 Jan 13	720.0	WIYN WHIRC H
Mrk 374	06 59 38.1	+54 11 48	0.04263	2016 May 21	2420.0	HST WFC3 F547M
Mrk 79	07 42 32.8	+49 48 35	0.02219	2006 Nov 08	2040.0	HST ACS HRC F550M
				2003 Aug 12	1500.0	MDM 1.3 m Templeton B
				2003 Aug 12	1965.0	MDM 1.3 m Templeton V
				2003 Aug 12	1110.0	MDM 1.3 m Templeton R
				2012 Jan 13	4140.0	WIYN WHIRC H
NGC 2617	08 35 38.8	−04 05 18	0.01421	2016 May 21	2230.0	HST WFC3 F547M
				2020 Feb 17	1020.0	APO 3.5 m ARCTIC B
				2020 Feb 17	840.0	APO 3.5 m ARCTIC V
				2020 Feb 17	450.0	APO 3.5 m ARCTIC R
NGC 3227	10 23 30.6	+19 51 54	0.00386	2010 Mar 29	2250.0	HST WFC3 F547M
				2003 Aug 12	1800.0	MDM 1.3 m Templeton B
				2003 Aug 12	2280.0	MDM 1.3 m Templeton V
				2003 Aug 12	1575.0	MDM 1.3 m Templeton R
				2013 Apr 26	1470.0	WIYN WHIRC H
SBS1116 + 583A	11 18 57.7	+58 03 24	0.02787	2010 Jun 06	2510.0	HST WFC3 F547M
NGC 3783	11 39 01.7	−37 44 19	0.00973	2011 Feb 09	2300.0	HST WFC3 F547M
				2015 Apr 23	960.0	SMARTS 0.9 m Tek2K B
				2015 Apr 23	960.0	SMARTS 0.9 m Tek2K V
				2015 Apr 23	960.0	SMARTS 0.9 m Tek2K R
Mrk 1310	12 01 14.3	−03 40 41	0.01956	2009 Dec 02	2240.0	HST WFC3 F547M
				2015 Apr 23	960.0	SMARTS 0.9 m Tek2K B
				2015 Apr 23	960.0	SMARTS 0.9 m Tek2K V
				2015 Apr 23	960.0	SMARTS 0.9 m Tek2K R
				2013 Apr 27	4500.0	WIYN WHIRC H
NGC 4051	12 03 09.6	+44 31 53	0.00234	2010 Jul 17	2340.0	HST WFC3 F547M
				2003 Aug 12	1250.0	MDM 1.3 m Templeton B
				2003 Aug 12	795.0	MDM 1.3 m Templeton V
				2003 Aug 12	690.0	MDM 1.3 m Templeton R
				2013 Apr 26	3060.0	WIYN WHIRC H
NGC 4151	12 10 32.6	+39 24 19	0.00332	2010 Jul 03	2310.0	HST WFC3 F547M
				2003 Aug 12	1470.0	MDM 1.3 m Templeton B
				2003 Aug 12	1200.0	MDM 1.3 m Templeton V
				2003 Aug 12	1370.0	MDM 1.3 m Templeton R
				2019 May 26	1800.0	ARCSAT SurveyCam I
				2013 Apr 27	1005.0	WIYN WHIRC H
NGC 4593	12 39 39.4	−05 20 39	0.00900	2010 Jul 10	2240.0	HST WFC3 F547M
				2003 Aug 12	1650.0	MDM 1.3 m Templeton B
				2003 Aug 12	1860.0	MDM 1.3 m Templeton V
				2003 Aug 12	1380.0	MDM 1.3 m Templeton R
				2013 Apr 27	960.0	WIYN WHIRC H
NGC 4748	12 52 12.4	−13 24 53	0.01463	2010 Jun 28	2250.0	HST WFC3 F547M
				2015 Apr 23	960.0	SMARTS 0.9 m Tek2K B
				2015 Apr 23	960.0	SMARTS 0.9 m Tek2K V
				2015 Apr 23	960.0	SMARTS 0.9 m Tek2K R
				2013 Apr 27	3600.0	WIYN WHIRC H
NGC 5548	14 17 59.5	+25 08 12	0.01718	2010 Jul 15	2260.0	HST WFC3 F547M
				2003 Nov 17	4000.0	MDM 1.3 m Templeton B
				2003 Nov 17	2500.0	MDM 1.3 m Templeton V
				2003 Nov 17	1380.0	MDM 1.3 m Templeton R
Mrk 817	14 36 22.1	+58 47 39	0.03146	2003 Dec 08	1020.0	HST ACS HRC F550M
				2003 Nov 04	2530.0	MDM 1.3 m Templeton B
				2003 Nov 04	1530.0	MDM 1.3 m Templeton V

Table 1
(Continued)

Target	R.A. (hh mm ss.s)	Decl. (dd mm ss)	z	Date (yyyy-mm-dd)	Exp Time (s)	Obs. Setup
				2003 Nov 04	930.0	MDM 1.3 m Templeton R
				2013 Apr 26	3520.0	WIYN WHIRC H
NGC 5940	15 31 18.1	+07 27 28	0.03393	2016 May 28	2230.0	HST WFC3 F547M
Mrk 290	15 35 52.3	+57 54 09	0.02958	2010 Jul 25	2520.0	HST WFC3 F547M
Zw 229-015	19 05 25.9	+42 27 40	0.02788	2014 Nov 13	2320.0	HST WFC3 F547M
1H1934-063	19 37 33.0	−06 13 05	0.01031	2016 May 27	2230.0	HST WFC3 F547M
				2015 Apr 23	960.0	SMARTS 0.9 m Tek2K B
				2015 Apr 23	960.0	SMARTS 0.9 m Tek2K V
				2015 Apr 23	960.0	SMARTS 0.9 m Tek2K R
NGC 6814	19 42 40.6	−10 19 25	0.00521	2010 May 06	2240.0	HST WFC3 F547M
				2019 Jun 23	1800.0	ARCSAT SurveyCam B
				2019 Jun 23	1800.0	ARCSAT SurveyCam V
				2019 Jun 23	1800.0	ARCSAT SurveyCam R
				2019 Jun 23	1800.0	ARCSAT SurveyCam I
				2011 Sep 20	1200.0	WIYN WHIRC H
NGC 7469	23 03 15.6	+08 52 26	0.01632	2009 Nov 11	2240.0	HST WFC3 F547M
				2003 Nov 13	1440.0	MDM 1.3 m Templeton B
				2003 Nov 13	1260.0	MDM 1.3 m Templeton V
				2003 Nov 13	1260.0	MDM 1.3 m Templeton R
				2019 Sep 28	70.0	APO 3.5 m ARCTIC I
				2011 Sep 19	300.0	WIYN WHIRC H

Section 3). For all ground-based data, images were reduced and combined in IRAF[8] following standard procedures.

2.2.1. Previous Observations

The majority of images used in this analysis were collected between 2003 and 2016 and have been previously described in publications. Table 1 lists observation dates, instrument setups, and exposure times.

HST. All 24 of our targets have medium-band V images obtained with the Hubble Space Telescope (HST). Galaxies were observed with either the Advanced Camera for Surveys (ACS) High Resolution Channel (HRC) through the F550M filter or the Wide Field Camera 3 (WFC3) through the F547M filter. The HRC has a field of view (FOV) of $29'' \times 26''$ and pixel scale of $0.025''$ pixel^{-1}. The WFC3 observations utilized the UVIS channel, which has a $160'' \times 160''$ FOV and pixel scale of $0.04''$ pixel^{-1}. In-depth descriptions of the HST observations and reductions are available in Bentz et al. (2009a, 2013), Bentz & Manne-Nicholas (2018).

WIYN. Eleven galaxies in our sample were imaged with the 3.5 m WIYN telescope[9] (NOAO 2011B-0120; PI: Bentz; NOAO 2013A-0438; PI: Manne-Nicholas). The observations employed the High-Resolution Infrared Camera (WHIRC) and the H filter. WHIRC is a 2048 × 2048 Raytheon Virgo HgCdTe, with a FOV of $202'' \times 202''$ and a pixel scale of $0.0986''$ pixel^{-1}. Each target was observed with multiple short exposures and large dither patterns to aid in the removal of strong fringing, cosmic rays, and bad pixels. A full description of the observations and reduction is available in Bentz & Manne-Nicholas (2018).

MDM. Eight galaxies were observed with the MDM Observatory 1.3 m McGraw-Hill Telescope. As described by Bentz et al. (2009b), objects were observed through Johnson B, V, and R filters with the Templeton CCD, which has 1024 × 1024 pixels, a pixel scale of $0.5''$ pixel^{-1}, and FOV of $8.49' \times 8.49'$.

2.2.2. New Observations

New imaging of galaxies in our sample was conducted between 2015 and 2020. Dates, instrument selections, and exposure times are listed in Table 1.

APO. We obtained B-, V-, R-, and I-band images of four galaxies in our sample with the 3.5 m Apache Point Observatory (APO) Astrophysical Research Consortium (ARC) telescope. The ARC Telescope Imaging Camera (ARCTIC) on the 3.5 m is a 4096 × 4096 pixel CCD with an FOV of $7.85' \times 7.85'$ and a pixel scale of $0.114''$ pixel^{-1}. Because unbinned imaging tends to oversample the seeing, we employed 2 × 2 binning for all objects imaged by ARCTIC, which yields an effective pixel scale of $0.228''$ pixel^{-1}.

SMARTS. Optical images of four galaxies were obtained with the Cerro Tololo Inter-American Observatory/Small and Moderate Aperture Research Telescope System (CTIO/SMARTS) 0.9 m telescope. The 0.9 m utilizes a 2048 × 2048 pixel CCD with an FOV of $13.6' \times 13.6'$ and pixel scale of $0.401''$ pixel^{-1}. Targets were observed through Tek2K Set II Johnson–Cousins B, V, and R filters.

ARCSAT. Using the 0.5 m ARC Small Aperture Telescope (ARCSAT), we targeted galaxies that had not been observed with APO, MDM, or SMARTS or did not have I-band imaging. ARCSAT employs the SurveyCam CCD imager, which has 4096 × 4096 pixels, an FOV of $31.1' \times 31.1'$, and pixel scale of $0.465''$ pixel^{-1}. For most observations, the large pixels and low spatial resolution caused the AGN and bulge to blend together in most images, eliminating the possibility of separation in the modeling process (see Section 3). The images

---

[8] IRAF is distributed by the National Optical Astronomy Observatory, which is operated by the Association of Universities for Research in Astronomy under a cooperative agreement with the National Science Foundation.

[9] The WIYN Observatory is a joint facility of the University of Wisconsin–Madison, Indiana University, the National Optical Astronomy Observatory and the University of Missouri.

for only two galaxies were found to be useful for surface brightness modeling; NGC 4151 and NGC 6814 were observed with Cousins *I* for the former and Johnson–Cousins *B*, *V*, *R*, and *I* for the latter. Dates and exposure times for these two galaxies are listed in Table 1.

3. Surface Brightness Modeling

As demonstrated by Bentz et al. (2013), up to 30% of the total galaxy brightness of nearby active galaxies may be contributed by a central AGN. The TF relation uses galaxy light as a mass tracer, thus accurate measurements of the galaxy starlight (which traces the stellar mass) are needed. In order to remove the AGN contamination from the host-galaxy brightness, we conducted two-dimensional surface brightness decompositions using GALFIT (Peng et al. 2002, 2010). For the vast majority of our targets, the decompositions of the *V*-band HST images have already been published (Bentz et al. 2009a, 2013; Bentz & Manne-Nicholas 2018). We follow a similar procedure here in the modeling of the new ground-based images.

GALFIT allows a galaxy image to be modeled by a combination of analytical surface brightness components. These components are not always physically meaningful, although they may correspond to the morphological components of each spiral galaxy (i.e., disks, bulges, bars, rings, etc.). We utilized the general Sérsic (1968) profile, which has the form

$$\sum(r) = \sum\nolimits_e \exp\left[-k\left(\left(\frac{r}{r_e}\right)^{1/n} - 1\right)\right], \tag{1}$$

where $\sum_e$ is the surface brightness of a pixel at an effective radius of r_e, n is the Sérsic index which dictates the profile's degree of curvature, and k is defined such that $\Gamma(2n) = 2\gamma(2n, k)$, where Γ and γ are the complete and incomplete gamma functions, respectively. The analytical profiles of the disks are extrapolated out to zero counts. The integrated magnitude of each component is calculated as $m = -2.5\log(\text{counts s}^{-1}) + zpt$, where m is the magnitude and zpt is the zero-point. A Sérsic index of $n = 1$ yields an exponential disk profile. Indices of $n = 0.5$ and $n = 4$ correspond to Gaussian and de Vaucouleurs (1948) profiles, respectively. Disks were modeled by holding the Sérsic index fixed at $n = 1$. Bulges are modeled with a typical index of $n > 1$, while bars are usually modeled by a shallower curvature of $n < 1$. For the few galaxies in our sample which displayed rings, we employed an exponential disk profile with the index fixed at $n = 1$ and truncation functions to remove the inner and outer regions of the profile.

The AGN in each galaxy is an unresolved point source, therefore the brightness can be constrained with an accurate model of the point-spread-function (PSF) of each image. The PSF models were built by first selecting an isolated star in the field, and then modeling a small portion of the image centered on the star. The star itself was modeled with a set of Gaussians whose widths, magnitudes, axis ratios, and position angles were left as free parameters, and the background sky was modeled as a gradient. A PSF model was considered suitable when the residuals, after subtracting the model from the image, contained only random noise. Evidence of regular patterns such as a "bull's-eye" signal the need for additional Gaussians. PSF models typically consisted of three to four Gaussian components. As we describe below, we fit several field stars in each image with the suitable PSF model in order to constrain the magnitude zero-point. When fit, the residuals of the field stars were small, demonstrating that any changes in the PSF shape across the FOV were minimal for the images considered here.

Once the PSF model was constructed, the entire galaxy image was modeled. The background sky was again modeled as a gradient across the frame. The unresolved AGN was fit with the PSF model, and the galaxy was fit with bulge and disk components. The surface brightness decompositions of the HST images, due to the higher spatial resolution, lower sky levels, and no seeing effects, were used to guide the number and type of components included in the decompositions of the ground-based images. Additional morphological components, such as a bar or ring, were included when present in the HST decompositions. Most bulge characteristics were fixed to the parameters determined from the HST image. This included radii, Sérsic indices, and axis ratios, while the magnitudes were left as free parameters. For very compact galaxies (e.g., Mrk 79, 1H1934-063), bar and ring parameters were also held fixed to their HST values. Field stars that were superimposed on or near the galaxy were also fit with the PSF model to fully isolate the galaxy brightness. Any saturated stars in the field were masked out before the fitting process began.

4. Measurements

With the surface brightness modeling complete and H I spectral data in hand, we discuss here the measurements conducted for use in TF distance determinations. These include the AGN-free, calibrated galaxy magnitudes and constraints on maximum rotational velocities from the H I emission lines.

4.1. Optical Galaxy Magnitudes

The TF relation for the optical bandpasses requires total, integrated galaxy magnitudes. Thus, with acceptable surface brightness models determined for each image, the image zero-points were then constrained in order to properly calibrate the model magnitudes. We achieved this by first modeling stars in the field that matched those in optical and near-infrared catalogs. The number of stars modeled was mainly dependent on how many were within the FOV, but was typically between 5 and 10. For all of our *B*- and *V*-band images, we drew stellar magnitudes from the AAVSO Photometric All-Sky Survey (APASS; Henden & Munari 2014; Henden et al. 2016), assuring none of the selected stars were flagged as variable. For NGC 6814 and Mrk 817, we utilized the *R*- and *I*-band field star magnitudes determined by Crimean Astrophysical Observatory imaging (Doroshenko et al. 2006).

For the remaining 12 galaxies in which data from the Crimean Observatory were not available, we collected *r*- and *i*-band stellar magnitudes first from the Sloan Digital Sky Survey (SDSS) data release 16 (Ahumada et al. 2020), or we collected the *r*- and *i*-band magnitudes from APASS. To transform the *r* and *i* magnitudes to *R* and *I*, we calculated synthetic photometry with the IRAF task SYNPHOT. We first estimated the spectral type of each star using the spectral classifications as a function of SDSS $g-i$ (using *g* stellar magnitudes from either SDSS or APASS) color from Table 4 of Covey et al. (2007). Once the spectral type was assigned, we employed the

Table 2
Galaxy Surface Brightness Parameters

Target (1)	$V_{\rm galaxy}$ (HST) (mag) (2)	$B_{\rm galaxy}$ (mag) (3)	$V_{\rm galaxy}$ (mag) (4)	$R_{\rm galaxy}$ (mag) (5)	$I_{\rm galaxy}$ (mag) (6)	$H_{-0.5,galaxy}$ (mag) (7)	Disk Radius (arcsec) (8)	q_d (9)
Mrk 1044	14.20 ± 0.20	⋯	13.96 ± 0.20	13.71 ± 0.20	12.76 ± 0.20	⋯	12.09 ± 0.78[a]	0.87
Ark 120	14.38 ± 0.20	⋯	⋯	⋯	⋯	11.85 ± 0.20	3.97 ± 0.56[b]	0.81
MCG+08-11-011	11.80 ± 0.20	⋯	⋯	⋯	⋯	⋯	56.84 ± 10.15[a]	0.62
Mrk 6	13.97 ± 0.20	⋯	13.74 ± 0.20	⋯	⋯	10.92 ± 0.20	29.45 ± 6.11[a]	0.61
Mrk 374	14.34 ± 0.20	⋯	⋯	⋯	⋯	⋯	8.47 ± 0.85[b]	0.58
Mrk 79	14.04 ± 0.20	14.22 ± 0.30	13.75 ± 0.20	13.25 ± 0.20	⋯	11.24 ± 0.20	31.68 ± 3.22[a]	0.79
NGC 2617	12.66 ± 0.20	14.10 ± 0.30	12.80 ± 0.20	12.51 ± 0.20	⋯	⋯	23.80 ± 8.61[a]	0.97
NGC 3227	11.00 ± 0.20	11.85 ± 0.20	10.87 ± 0.20	10.48 ± 0.20	⋯	8.22 ± 0.20	91.57 ± 18.72[a]	0.42
SBS1116 + 583A	15.57 ± 0.20	⋯	⋯	⋯	⋯	13.65 ± 0.20	3.14 ± 0.44[b]	0.87
NGC 3783	12.09 ± 0.20	12.89 ± 0.20	12.03 ± 0.20	11.50 ± 0.20	⋯	⋯	58.39 ± 6.58[a]	0.96
Mrk 1310	14.93 ± 0.20	⋯	15.02 ± 0.20	14.40 ± 0.20	⋯	12.47 ± 0.20	11.67 ± 1.19[a]	0.73
NGC 4051	10.11 ± 0.20	10.84 ± 0.20	10.21 ± 0.20	9.93 ± 0.20	⋯	8.57 ± 0.20	127.67 ± 7.22[a]	0.58[c]
NGC 4151	10.80 ± 0.20	11.29 ± 0.20	10.63 ± 0.20	10.18 ± 0.20	9.73 ± 0.20	9.01 ± 0.20	64.12 ± 6.00[a]	0.94[d]
NGC 4593	11.21 ± 0.20	12.05 ± 0.20	11.21 ± 0.20	10.70 ± 0.20	⋯	9.46 ± 0.20	89.44 ± 19.00[a]	0.69[c]
NGC 4748	13.56 ± 0.20	14.43 ± 0.30	13.19 ± 0.30	12.54 ± 0.20	⋯	10.94 ± 0.20	24.46 ± 5.46[a]	0.69
NGC 5548	12.72 ± 0.20	13.39 ± 0.20	12.58 ± 0.20	12.24 ± 0.20	⋯	⋯	36.03 ± 3.35[a]	0.83
Mrk 817	14.30 ± 0.20	15.04 ± 0.30	13.99 ± 0.30	13.58 ± 0.30	⋯	11.76 ± 0.20	13.03 ± 2.12[a]	0.81
Mrk 478	15.54 ± 0.20	⋯	⋯	⋯	⋯	⋯	3.39 ± 0.34[b]	0.85
NGC 5940	13.35 ± 0.20	⋯	⋯	⋯	⋯	⋯	9.21 ± 0.92[b]	0.86
Mrk 290	15.31 ± 0.20	⋯	⋯	⋯	⋯	⋯	4.12 ± 0.41[b]	0.81
Zw 229-015	15.08 ± 0.20	⋯	⋯	⋯	⋯	12.77 ± 0.20	9.31 ± 1.33[b]	0.60
1H1934-063	13.16 ± 0.20	14.47 ± 0.20	13.59 ± 0.20	13.08 ± 0.20	⋯	⋯	22.90 ± 3.12[a]	0.85
NGC 6814	11.18 ± 0.20	12.16 ± 0.30	11.22 ± 0.20	10.62 ± 0.20	9.91 ± 0.20	9.80 ± 0.20	66.91 ± 15.75[a]	0.98
NGC 7469	12.51 ± 0.20	13.05 ± 0.20	12.29 ± 0.20	12.10 ± 0.20	11.12 ± 0.20	9.84 ± 0.20	33.44 ± 2.03[a]	0.81

Notes. Total calibrated galaxy magnitudes after removal of AGN contamination. Full decomposition information of the HST galaxy images is available in Bentz & Manne-Nicholas (2018). The majority of the surface brightness fits to the ground-based images were guided by the HST-based solutions (see Section 3). The B, V, R, and I magnitudes are total magnitudes, the $H_{-0.5}$ magnitude is calibrated for the aperture system of Aaronson et al. (1980). Disk axis ratios (q_d) are adopted from the HST decompositions of Bentz & Manne-Nicholas (2018) unless otherwise noted. Disk radii are either measured at the B-band 25th mag arcsec^{-2} isophote (R_{25}) or derived from the exponential disk radii (R_d) as noted. Uncertainties on the magnitudes were determined based on the quality of the surface brightness fits (see Section 4.1).

[a] Radius at the B-band 25th mag arcsec^{-2} isophote (see Section 5).

[b] Derived from the exponential disk radii (see Section 3).

[c] Averaged from ground-based decompositions.

[d] Derived from the inclination of the resolved H I disk (Mundell et al. 1995).

corresponding stellar template from the Kurucz 1993 Atlas of Model Atmospheres (Kurucz 1993), and used SYNPHOT to calculate the difference between magnitudes of the template through the SDSS and Johnson–Cousins throughputs. The color differences were small for R and r, $-0.05 < m_R - m_r < -0.26$, and slightly larger for I and i, $-0.06 < m_I - m_i < -0.76$.

We adjusted the zero-point in GALFIT to minimize the difference between the measured and expected magnitudes of the field stars, thus calibrating the photometry of the galaxy components as well. Lastly, we combined all the host-galaxy surface brightness components to determine total galaxy magnitudes, which are listed in Table 2.

We determine a typical uncertainty of 0.2 mag for the integrated galaxy magnitudes, consistent with Bentz & Manne-Nicholas (2018) based on our previous experience using GALFIT as well as the level of agreement between fitting results to HST images of compact PG quasars (Veilleux et al. 2009). In some cases, poor seeing conditions or bright sky background induced higher uncertainty in the separation of AGN light from bulge light, or disk light from the sky contribution. For these cases, we assigned a slightly larger uncertainty of 0.3 mag to the final galaxy magnitudes (Mrk 79, NGC 2617 NGC 4748, Mrk 817, NGC 6814). We were unable to separate the disk light from sky contribution in the B-band images of Mrk 1044 and Mrk 6. Additionally for Mrk 1310, the seeing conditions coupled with focusing offsets in the B-band image caused substantial blending of the AGN and bulge light, thus we were unable to remove the AGN contamination. For these three galaxies, we omit the B-band data from our analysis.

Figure 1 displays selected B-band galaxy images, surface brightness models, and residuals, which show the range of quality in our surface brightness models of the ground-based images. For the most extended galaxies, like NGC 4593 and NGC 3783 (first and second column, respectively), we have good surface brightness models due to the larger size of the galaxy on the detector and hence, easier separation of each surface brightness component in the modeling process. More compact galaxies like NGC 4748 (third column) had surface brightness models of moderate quality, and the most compact galaxies, such as Mrk 817 (fourth column), had relatively poor quality surface brightness models. The quality of our models was mainly determined by comparing our galaxy V-band magnitudes to their HST V-band magnitudes. Good models had excellent agreement, usually within ∼0.01–0.02 mag. While moderate and poor models had larger discrepancies (∼0.1–0.3 mag), they are still in agreement within the larger uncertainties attributed to the compactness of the galaxy and

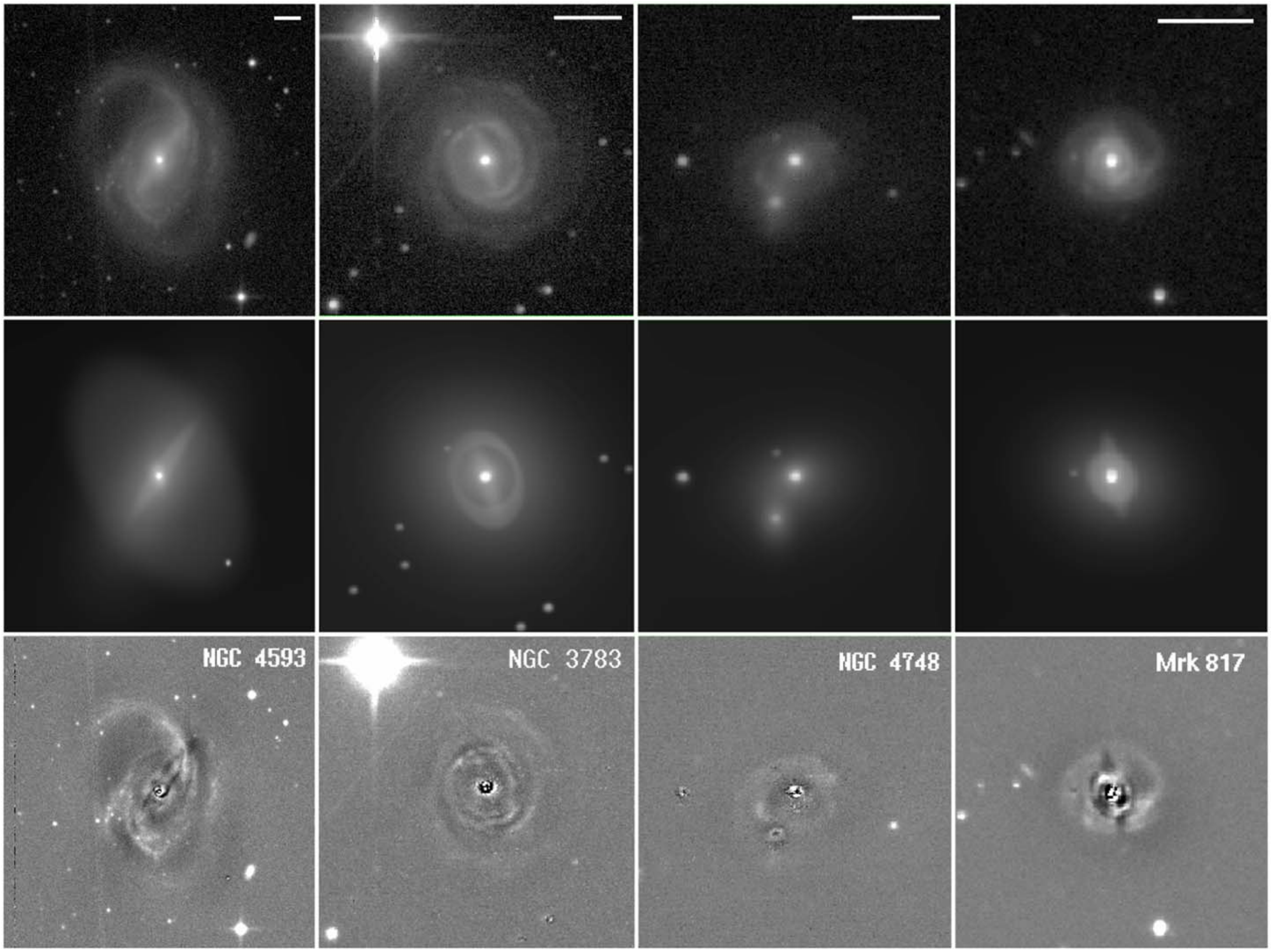

Figure 1. Selected ground-based B-band AGN host-galaxy images (top), GALFIT models (center), and residuals (bottom). From left to right: NGC 4593, NGC 3783, NGC 4748, Mrk 817. The images and models are displayed with a logarithmic stretch, and the residuals are displayed with a linear stretch centered around zero counts. The scale bars in each row are 30″ in length. Due to the varying levels of compactness of each galaxy, the selected fits correspond to the quality range of the separation of the AGN and galaxy light, from good (NGC 4593, NGC 3783), to moderate (NGC 4748), to poor (Mrk 817). Higher uncertainties were assigned to galaxies with poor fits (see Section 4.1 for a quantitative explanation). Magnitudes were calculated as $m = -2.5\log(\text{counts s}^{-1}) + zpt$.

the seeing conditions that complicated the modeling process of the ground-based images.

4.2. H-*band Aperture Photometry*

The TF relation for the H band utilizes the $H_{-0.5}$ magnitude, which is calibrated for the aperture system $\log(A/D_{25}^{i}) = -0.5$, where A is the aperture through which the galaxy intensity is measured and D_{25}^{i} is the galaxy diameter at the B-band 25 mag arcsec^{-2} isophote, corrected for inclination (Aaronson et al. 1980). We employed the ELLIPSE task in IRAF to measure isophotes from our sky-subtracted, ground-based B-band images, with Galactic extinction corrections applied to the B-band magnitudes. We then fit an exponential disk function to the outer surface brightness profile to arrive at the semimajor axis in arcseconds at which the surface brightness reached 25 mag arcsec^{-2}. An example is shown in Figure 2, where the blue dashed line indicates the 25th mag arcsec^{-2} surface brightness. For galaxies that had H-band imaging but did not have B-band images (Ark 120, SBS1116+583A, Zw 229-015), we utilized the relation between the radius at the 25 mag arcsec^{-2} isophote (R_{25}) and the exponential disk scale length (R_d) of $R_{25} = 3.2\ R_d$ (Catinella et al. 2006; de Blok & Walter 2014) to estimate D_{25} from our exponential disk profile fits. Lastly, our inclination corrections to the diameters follow the formula from the Second Reference Catalog of Bright Galaxies (de Vaucouleurs et al. 1976):

$$D_{25}^{i} = D_{25}(a/b)^{-C}, \qquad (2)$$

where a/b is the ratio of major to minor axes, and Tully & Fouque (1985) determined $C = 0.22 \pm 0.03$ based on their best fit to the deviations in H-band surface brightness as a function of galaxy inclination. $H_{-0.5}$-band magnitudes in addition to the galaxy radii and corresponding measurement method are listed in Table 2.

Aaronson et al. (1980) originally assumed a typical uncertainty of 0.1 mag for their $H_{-0.5}$-band values. However, the aperture photometry for our sample was conducted on galaxy images in which we removed the AGN contamination in the surface brightness modeling process, which induces additional uncertainty in the total galaxy magnitude. Therefore,

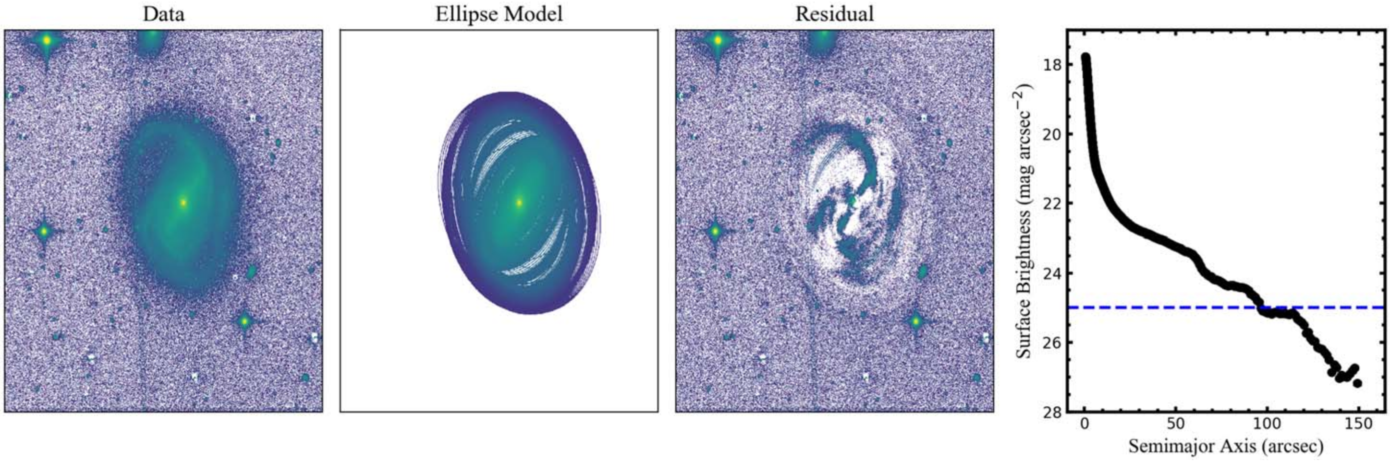

Figure 2. From left to right: original *B*-band image of NGC 4593, surface brightness isophotes from the ELLIPSE task in IRAF, data minus the model, and the surface brightness measurements as a function of semimajor axis in arcseconds. The 25 mag arcsec^{-2} surface brightness is indicated with the blue dashed line. East is up and north is right in the above images, and the FOV is 7.78′ × 8.49′.

we conservatively adopt 0.2 mag uncertainty on all $H_{-0.5}$ magnitudes, consistent with our typical uncertainties on the AGN-free galaxy magnitudes for the optical bands.

4.3. H I 21 cm Line Widths

The TF relation utilizes the width of the unresolved, rotationally broadened H I 21 cm emission line from late-type galaxies, which is directly related to the maximum rotation rate (Epstein 1964; Roberts 1969). We follow the method originally described by Tully & Fouque (1985), with the updated definition of the H I line width (Courtois et al. 2009), which includes corrections for instrumental and redshift broadening:

$$W_{m50}^{c} = \frac{W_{m50}}{(1+z)} - 2\Delta v\lambda, \tag{3}$$

where z is the redshift of the H I line, Δv is the smoothed resolution of the spectrum, and λ is an empirically determined constant term given as $\lambda = 0.25$. We use the redshifts of the H I lines of our targets reported in Paper I. W_{m50} is defined as the width of the H I profile at 50% of the mean flux over the range of spectral channels, which contain 90% of the H I flux. This new definition by Courtois et al. (2009) is preferred as it employs the mean flux rather than the peak, which makes the width measurement independent of the strengths of the flanks. Excluding 5% of the flux on either side of the profile also aids in separation of the profile wings from the noise. The line widths reported in Paper I are widths calculated at 50% and 20% over 100% of the flux. Therefore, we have remeasured the widths of our H I profiles using the updated definition and we list them in Table 3. An example of this measurement for the H I emission from NGC 4593 is shown in Figure 3.

The corrected, observed width is then adjusted to agree statistically with twice the maximum rotational velocity, as the width of the H I line includes both redshifted and blueshifted gas motions. The translation is given as

$$\begin{aligned} W_{\rm mx}^{2} &= (W_{m50}^{c})^{2} + (W_{t,m50})^{2}[1 - 2e^{-(W_{m50}^{c}/W_{c,m50})^{2}}] \\ &\quad - 2W_{m50}^{c}W_{t,m50}[1 - e^{-(W_{m50}^{c}/W_{c,m50})^{2}}], \end{aligned} \tag{4}$$

where $W_{c,m50} = 100\ {\rm km\ s^{-1}}$ and $W_{t,m50} = 9\ {\rm km\ s^{-1}}$ are the values found by Courtois et al. (2009) to produce the best match between maximum rotation rate and adjusted H I line width. The width is then deprojected to edge-on orientation by

$$W_{\rm mx}^{i} = W_{\rm mx}/sin(i), \tag{5}$$

where i is the inclination of the galaxy disk.

The inclinations were generally derived from the axis ratios of the galaxy disk, as listed in Table 2. For most of the galaxies, we adopted the axis ratios reported by Bentz & Manne-Nicholas (2018). For NGC 4051 and NGC 4593, where the disk extended beyond the FOV of the HST image, we adopted the axis ratios from our GALFIT models of the ground-based images. For NGC 4151, the spatially resolved H I study by Mundell et al. (1999) reveals the inclination of the H I disk to be 21°, much more face-on than the disk axis ratio that has been typically found in the optical based on the high surface brightness stellar distribution (∼0.6; de Vaucouleurs et al. 1976, 1991; Bentz & Manne-Nicholas 2018; see Section 5.4). We therefore adopt 21° as the true inclination of the H I disk for NGC 4151. We follow the standard prescription from the photo-visual analysis of Holmberg (1958) adopted by the main TF works in the literature (Tully & Fisher 1977; Tully & Pierce 2000; Tully et al. 2008, 2013):

$$\cos(i) = [(q_{d}^{2} - q_{0,d}^{2})\big/(1 - q_{0,d}^{2})]^{1/2}, \tag{6}$$

where $q_d = b/a$ is the disk axis ratio and $q_{0,d}$ is the intrinsic axial ratio of a disk galaxy viewed edge-on. Following Tully & Pierce (2000), we adopt $q_{0,d} = 0.2$ as the single, global value for the flattening. The uncertainties in the deprojected line widths increase as galaxy inclinations become more face-on. Consequently, the galaxies in this sample with the lowest inclination (NGC 2617, NGC 3783, NGC 6814) have the highest uncertainties in $W_{\rm mx}^{i}$.

5. TF Distances

With H I widths in hand and the AGN contamination removed from the galaxy brightness, we employed the TF method to constrain the distance to each AGN host.

Table 3
21 cm Spectral Characteristics

Target (1)	V_R (km s^{-1}) (2)	$W_{\rm m50}$ (km s^{-1}) (3)	S/N (4)	Flux (Jy km s^{-1}) (5)	Resolution (km s^{-1}) (6)
Mrk 1044	4912.0	178.0 ± 8.0	20.4	4.98	1.1
Ark 120	9810.0	350.0 ± 13.0	10.1	3.63	2.4
MCG+08-11-011	6132.0	309.0 ± 8.0	28.7	14.97	0.8
Mrk 6	5632.0	477.0 ± 19.0	2.6	3.31	3.3
Mrk 374	13246.0	271.0 ± 18.0	4.6	0.60	9.0
Mrk 79	6661.0	178.0 ± 12.0	11.4	5.71	3.4
NGC 2617	4265.0	119.0 ± 8.0	41.7	18.62	0.3
NGC 3227	1148.0	428.0 ± 9.0	14.8	29.87	3.2
SBS1116+583A	8373.0	168.0 ± 18.0	3.8	0.43	6.8
NGC 3783	2916.0	147.0 ± 8.0	31.0	21.03	0.7
Mrk 1310	5838.0	258.0 ± 15.0	7.5	2.38	3.4
NGC 4051	703.0	245.0 ± 8.0	147.2	61.59	0.6
NGC 4151	999.0	131.0 ± 8.0	45.4	74.4	0.6
NGC 4593	2502.0	370.0 ± 9.0	15.4	13.52	0.7
NGC 4748	4184.0	332.0 ± 15.0	8.0	2.79	2.0
NGC 5548	5150.0	212.0 ± 15.0	8.2	2.12	5.3
Mrk 817	9438.0	353.0 ± 19.0	3.1	0.74	8.2
Mrk 478	23881.0	314.0 ± 23.0	1.9	0.73	8.8
NGC 5940	10209.0	186.0 ± 13.0	10.6	3.33	1.3
Mrk 290	9104.0	245.0 ± 18.0	3.8	0.76	6.8
Zw 229-015	8317.0	209.0 ± 17.0	5.2	0.94	6.4
1H1934-063	3191.0	165.0 ± 10.0	13.6	4.54	2.0
NGC 6814	1562.0	84.0 ± 8.0	60.4	55.92	0.2
NGC 7469	4930.0	215.0 ± 16.0	6.1	2.00	3.3

Note. Columns 2 and 3 list the measured recessional velocity and W_{m50} values, respectively, with the updated H I line width measurement method described in Section 5. Columns 4 and 5 list the signal-to-noise ratio (S/N) and flux after spectral smoothing to the final spectral resolution, reported in Column 6.

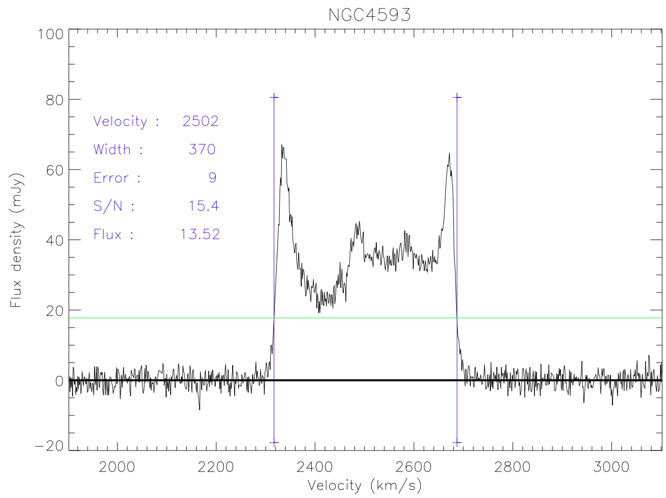

Figure 3. Example of the W_{m50} line width measurement method for the H I emission spectrum of NGC 4593. The blue vertical lines indicate the range of spectral channels that contain 90% of the H I flux, while the green horizontal line indicates 50% of the mean flux in this range. The integrated flux measurement is in units of Jy km s^{-1}, and the width and velocity measurements are in units of kms^{-1}. The error is the uncertainty on the width and in units of kms^{-1}.

5.1. Current TF Calibrations

The current calibrations for the B, R, $H_{-0.5}$ (Tully et al. 2008), and I-band (Tully & Courtois 2012) TF relations are as follows:

$$M_B^{b,i,k} = -19.99 - 7.27(\log W_{\rm mx}^i - 2.5), \tag{7}$$

$$M_R^{b,i,k} = -21.00 - 7.65(\log W_{\rm mx}^i - 2.5), \tag{8}$$

$$M_I^{b,i,k} = -21.39 - 8.81(\log W_{\rm mx}^i - 2.5), \tag{9}$$

$$M_{H_{-0.5}}^{b,i,k} = -22.17 - 9.55(\log W_{\rm mx}^i - 2.5), \tag{10}$$

where b, i, and k are the Galactic extinction, inclination, and redshift corrections, respectively, and the superscripts on the magnitudes indicate that the corresponding corrections have been applied. We estimate the extinction along the line of sight in each bandpass using the Schlafly & Finkbeiner (2011) recalibration of the Milky Way dust map of Schlegel et al. (1998).

The inclination correction is given by the expression $A_i^\lambda = \gamma_\lambda \log(a/b)$, originally formulated by Tully et al. (1998) and subsequently used by Tully et al. (2008) and Tully & Courtois (2012), where λ is the passband, a/b is the ratio of major to minor axes of the galaxy disk, and γ is defined as

$$\gamma_B = 1.57 + 2.75(\log W_{\rm mx}^i - 2.5), \tag{11}$$

$$\gamma_R = 1.15 + 1.88(\log W_{\rm mx}^i - 2.5), \tag{12}$$

$$\gamma_I = 0.92 + 1.63(\log W_{\rm mx}^i - 2.5). \tag{13}$$

However, Tully et al. (1998) do not include a prescription for the $H_{-0.5}$ magnitudes. Sakai et al. (2000) approximated the correction as $A_i^{H_{-0.5}} = 0.5A_i^I$, however, we adopt the original correction from Tully & Fouque (1985) of $A_i^{H_{-0.5}} = 0.1A_i^B$ as it was derived from measurements in the $H_{-0.5}$ band.

Finally, the k-corrections for the B, R, and I bands utilized in the TF calibrations of Tully et al. (2008) and Tully & Courtois (2012) are described in Tully & Pierce (2000) and Chilingarian et al. (2010) for the optical bands and near-infrared band,

Table 4
Corrected H I Line Widths and Magnitudes

Target (1)	Morphology (2)	$W^i_{\rm mx}$ (3)	$m_V^{b,i,k}$ (HST) (4)	$m_B^{b,i,k}$ 5	$m_V^{b,i,k}$ (6)	$m_R^{b,i,k}$ (7)	$m_I^{b,i,k}$ (8)	$m_{H_{-0.5}}^{b,i,k}$ (9)
Mrk 1044	SB(s)c	329.89 ± 28.33	14.02 ± 0.20	⋯	13.79 ± 0.20	13.56 ± 0.20	12.65 ± 0.20	⋯
Ark 120	Sb pec	549.21 ± 33.78	13.82 ± 0.20	⋯	⋯	⋯	⋯	11.71 ± 0.20
MCG+08-11-011	SBc	360.16 ± 11.95	10.93 ± 0.20	⋯	⋯	⋯	⋯	⋯
Mrk 6	Sb	565.76 ± 25.94	13.19 ± 0.20	⋯	12.96 ± 0.20	⋯	⋯	10.78 ± 0.20
Mrk 374	SBc	295.93 ± 22.24	13.93 ± 0.20	⋯	⋯	⋯	⋯	⋯
Mrk 79	SBb	261.91 ± 21.85	13.74 ± 0.20	13.77 ± 0.30	13.45 ± 0.20	12.95 ± 0.20	⋯	11.15 ± 0.20
NGC 2617	Sc	445.10 ± 149.27	12.53 ± 0.20	13.93 ± 0.30	12.68 ± 0.20	12.38 ± 0.20	⋯	⋯
NGC 3227	SAB(s) pec	448.88 ± 10.74	10.38 ± 0.20	11.00 ± 0.20	10.25 ± 0.20	9.85 ± 0.20	⋯	8.13 ± 0.20
SBS1116 + 583A	SBc	301.51 ± 41.10	15.45 ± 0.20	⋯	⋯	⋯	⋯	13.58 ± 0.20
NGC 3783	(R')SB(r)a	480.53 ± 120.76	11.71 ± 0.20	12.38 ± 0.20	11.65 ± 0.20	11.17 ± 0.20	⋯	⋯
Mrk 1310	Sbc	347.49 ± 24.08	14.67 ± 0.20	⋯	14.76 ± 0.20	14.13 ± 0.20	⋯	12.40 ± 0.20
NGC 4051	SAB(rs)bc	282.83 ± 15.66	9.87 ± 0.20	10.45 ± 0.20	9.97 ± 0.20	9.61 ± 0.20	⋯	8.52 ± 0.20
NGC 4151	(R')SAB(rs)ab	342.95 ± 56.31	10.69 ± 0.20	11.14 ± 0.20	10.52 ± 0.20	10.09 ± 0.20	9.66 ± 0.20	8.98 ± 0.20
NGC 4593	(R)SB(rs)b	437.95 ± 23.30	10.81 ± 0.21	11.51 ± 0.20	10.81 ± 0.20	10.29 ± 0.20	⋯	9.39 ± 0.20
NGC 4748	Sab	429.70 ± 23.25	13.17 ± 0.20	13.89 ± 0.30	12.80 ± 0.30	12.17 ± 0.20	⋯	10.86 ± 0.20
NGC 5548	(R')SA(s)0/a	534.08 ± 30.90	12.49 ± 0.20	13.08 ± 0.20	12.35 ± 0.20	12.03 ± 0.20	⋯	⋯
Mrk 817	SBc	549.93 ± 40.97	14.09 ± 0.20	14.76 ± 0.30	13.78 ± 0.30	13.38 ± 0.30	⋯	11.67 ± 0.20
Mrk 478	Sab	516.02 ± 163.75	15.24 ± 0.22	⋯	⋯	⋯	⋯	⋯
NGC 5940	SBc	327.54 ± 32.79	13.13 ± 0.20	⋯	⋯	⋯	⋯	⋯
Mrk 290	S0	376.64 ± 34.87	15.08 ± 0.20	⋯	⋯	⋯	⋯	⋯
Zw 229-015	(R)SBc	234.32 ± 21.15	14.71 ± 0.20	⋯	⋯	⋯	⋯	12.66 ± 0.20
1H1934-063	Sbc	286.26 ± 25.28	12.29 ± 0.20	13.30 ± 0.20	12.72 ± 0.20	12.33 ± 0.20	⋯	⋯
NGC 6814	SAB(rs)bc	388.09 ± 195.55	10.66 ± 0.20	11.46 ± 0.30	10.69 ± 0.20	10.20 ± 0.21	9.62 ± 0.20	9.71 ± 0.20
NGC 7469	(R')SAB(rs)a	335.80 ± 30.96	12.19 ± 0.20	12.60 ± 0.20	11.97 ± 0.20	11.83 ± 0.20	10.92 ± 0.20	9.76 ± 0.20

Note. The morphological classifications listed in Column 2 are consistent with those reported from Paper I. Column 3 lists the corrected H I line width in kilometers per second, which is statistically equal to twice the maximum rotation rate, deprojected to edge-on orientation (see Section 4.3). Columns 4–8 list the observed magnitudes in each band corrected for Galactic extinction, inclination-dependent extinction, and redshift (see Sections 5.1, 5.2).

respectively, and are as follows:

$$A_k^B = (3.6 - 0.36T)z, \tag{14}$$

$$A_k^R = [4.24(R - I) - 1.10]z, \tag{15}$$

$$A_k^I = 0.302z + 8.768z^2 - 68.680z^3 + 181.904z^4, \tag{16}$$

where T is the galaxy morphological type (1, 3, 5, and 7 corresponding to Sa, Sb, Sc, and Sd) and z is the redshift. The k-corrections in this work utilize the morphological classifications reported in Paper I and are listed in Table 4. Once more the $H_{-0.5}$ band lacks a prescription from Tully & Pierce (2000), thus we adopt the original k-correction from Aaronson et al. (1980) as $A_k^{H_{-0.5}} = 1.9z$.

5.2. V-*band TF Calibration*

The TF relation has been calibrated for most optical and near-infrared bands (Tully et al. 2008; Tully & Courtois 2012), and most recently for SDSS and Wide-field Infrared Survey Explorer filters (Kourkchi et al. 2020). However, the Johnson V band has so far been neglected. We have therefore conducted the first calibration of the V-band TF relation.

We began by identifying the galaxies that were used to calibrate the most recent definitions of the optical TF relations (Tully et al. 2008). These included galaxies with distances determined from either Cepheid variable stars (26 galaxies), TRGB stars (13 galaxies), or SBF (7 galaxies). We then retrieved the V-band magnitudes for these galaxies from the Third Reference Catalogue of Bright Galaxies (RC3; de Vaucouleurs et al. 1991), the same source for the B-band magnitudes from the calibrations of Tully et al. (2008). These are purely observed magnitudes that have not been corrected for Galactic extinction, inclination-dependent extinction, or redshift. We followed Tully et al. (2008) and adopted the Schlegel et al. (1998) extinction corrections. We derived the inclination-dependent and redshift corrections in the V band following the same methods used to define them in B, R, and I. In-depth descriptions of the corrections and final calibration are available in the Appendix.

Tully et al. (1998) detailed the extinction corrections due to inclination in the B, R, and I bands. Following the same procedure and adopting the same formalism for the extinction parameter, $A_i^\lambda = \gamma_\lambda \log(a/b)$, where a/b is inverse of the disk axis ratio, we find

$$\gamma_V = (1.01 \pm 4.06) + (2.94 \pm 1.09)(\log W_{\rm R}^i - 2.5). \tag{17}$$

The method for deriving the k-corrections adopted by Tully & Pierce (2000) is not described, however, they are quite similar to the k-corrections based on the analysis of Frei & Gunn (1994). We therefore adopt the Frei & Gunn (1994) methodology and find a V-band k-correction of

$$A_k^V = (2.23 - 0.22T)z, \tag{18}$$

where T is the morphological type (1, 3, 5, and 7 again corresponding to Hubble types Sa, Sb, Sc, and Sd) and z is the redshift.

The extinction, inclination, and k-corrections were then applied to the apparent V magnitudes from RC3 of the Tully et al. (2008) calibrating sample. Using the accurate distances to these galaxies, which are based on Cepheids, TRGB, or SBF, we derived their absolute magnitudes. Finally, we fit a linear relationship between the absolute magnitudes and the H I line

Table 5
TF Distance and $V_{\rm PEC}$ Measurements

Target	Band	D (Mpc)	$V_{\rm PEC}$ (km s^{-1})	Flag
Mrk 1044	V (HST)	81.3 ± 13.0	…	…
	V	73.0 ± 11.7	…	…
	R	86.9 ± 14.0	…	…
	I	69.1 ± 12.2	…	…
	Best estimate	81.3 ± 16.3	−1275 ± 1212	a
Ark 120	V (HST)	161.2 ± 21.2	…	…
	$H_{-0.5}$	171.4 ± 25.6	…	…
	Best estimate	161.2 ± 32.2	−1855 ± 2394	a
MCG+08-11-011	V (HST)	22.4 ± 4.5	4586 ± 335	c
Mrk 6	V (HST)	126.2 ± 14.7	…	…
	V	113.6 ± 13.2	…	…
	$H_{-0.5}$	117.9 ± 15.0	…	…
	Best estimate	126.2 ± 25.2	−3625 ± 1873	b
Mrk 374	V (HST)	66.1 ± 13.2	8878 ± 981	c
Mrk 79	V (HST)	50.2 ± 7.9	…	…
	B	42.9 ± 7.9	…	…
	V	43.9 ± 6.9	…	…
	R	46.3 ± 7.3	…	…
	$H_{-0.5}$	32.2 ± 5.9	…	…
	Best estimate	50.2 ± 10.0	3181 ± 743	b
NGC 2617	V (HST)	64.7 ± 33.6	…	…
	B	100.0 ± 50.7	…	…
	V	69.1 ± 35.9	…	…
	R	79.9 ± 41.7	…	…
	Best estimate	64.7 ± 19.5	−183 ± 1446	a
NGC 3227	V (HST)	24.3 ± 2.4	…	…
	B	26.3 ± 2.6	…	…
	V	22.9 ± 2.3	…	…
	R	25.3 ± 2.5	…	…
	$H_{-0.5}$	22.4 ± 2.3	…	…
	Best estimate	24.3 ± 4.9	−323 ± 364	a
SBS1116 + 583A	V (HST)	136.7 ± 31.1	…	…
	$H_{-0.5}$	129.0 ± 35.6	…	…
	Best estimate	136.7 ± 27.3	−1393 ± 2030	a
NGC 3783	V (HST)	49.8 ± 19.6	…	…
	B	54.8 ± 20.7	…	…
	V	48.5 ± 19.1	…	…
	R	51.6 ± 20.4	…	…
	Best estimate	49.8 ± 10.0	−427 ± 743	a
Mrk 1310	V (HST)	118.7 ± 16.7	…	…
	V	123.4 ± 17.3	…	…
	R	122.7 ± 17.3	…	…
	$H_{-0.5}$	98.3 ± 15.8	…	…
	Best estimate	118.7 ± 23.7	−2480 ± 1762	b
NGC 4051	V (HST)	9.5 ± 1.2	…	…
	B	10.4 ± 1.1	…	…
	V	10.0 ± 1.1	…	…
	R	11.2 ± 1.2	…	…
	$H_{-0.5}$	11.1 ± 1.3	…	…
	Best estimate	9.5 ± 1.9	227 ± 141	a
NGC 4151	V (HST)	18.6 ± 5.0	…	…
	B	18.9 ± 4.8	…	…
	V	17.2 ± 4.6	…	…
	R	18.7 ± 5.0	…	…
	I	18.7 ± 5.7	…	…
	$H_{-0.5}$	19.9 ± 6.5	…	…
	Best estimate	18.6 ± 3.7	−127 ± 275	a
NGC 4593	V (HST)	28.5 ± 3.6	…	…
	B	32.0 ± 3.3	…	…
	V	28.6 ± 3.0	…	…
	R	29.9 ± 3.1	…	…
	$H_{-0.5}$	38.2 ± 4.2	…	…
	Best estimate	28.5 ± 5.7	756 ± 424	a
NGC 4748	V (HST)	82.2 ± 10.2	…	…
	B	93.2 ± 14.9	…	…
	V	69.3 ± 11.2	…	…
	R	68.7 ± 8.5	…	…
	$H_{-0.5}$	72.3 ± 10.0	…	…
	Best estimate	82.2 ± 16.4	−1513 ± 1219	b
NGC 5548	V (HST)	83.6 ± 10.7	…	…
	B	88.0 ± 11.0	…	…
	V	78.4 ± 10.0	…	…
	R	90.0 ± 11.5	…	…
	Best estimate	83.6 ± 16.7	−753 ± 1242	a
Mrk 817	V (HST)	182.8 ± 26.8	…	…
	B	198.9 ± 35.0	…	…
	V	158.7 ± 28.4	…	…
	R	175.0 ± 31.4	…	…
	$H_{-0.5}$	168.8 ± 28.6	…	…
	Best estimate	182.8 ± 36.6	−3770 ± 2721	c
Mrk 478	V (HST)	282.2 ± 139.4	4655 ± 10323	c
NGC 5940	V (HST)	53.4 ± 10.7	6687 ± 795	c
Mrk 290	V (HST)	162.3 ± 32.5	−2644 ± 2416	a
Zw 229-015	V (HST)	66.3 ± 11.0	…	…
	$H_{-0.5}$	52.2 ± 10.2	…	…
	Best estimate	66.3 ± 13.3	3424 ± 989	c
1H1934-063	V (HST)	29.5 ± 4.8	…	…
	B	39.3 ± 6.2	…	…
	V	36.0 ± 5.9	…	…
	R	39.3 ± 6.4	…	…
	Best estimate	29.5 ± 5.9	818 ± 439	a
NGC 6814	V (HST)	22.1 ± 17.1	…	…
	B	26.3 ± 19.6	…	…
	V	22.5 ± 17.4	…	…
	R	23.8 ± 18.5	…	…
	I	22.9 ± 20.4	…	…
	$H_{-0.5}$	35.1 ± 33.9	…	…
	Best estimate	22.1 ± 8.0	−283 ± 593	a
NGC 7469	V (HST)	36.0 ± 6.1	…	…
	B	36.0 ± 5.9	…	…
	V	32.5 ± 5.5	…	…
	R	40.4 ± 6.8	…	…
	I	32.3 ± 6.0	…	…
	$H_{-0.5}$	27.3 ± 5.4	…	…
	Best estimate	36.0 ± 7.2	1949 ± 535	c

Note. TF Distance and $V_{\rm PEC}$ measurements for all bands. We quote the distance predicted from our V-band TF calibration of the HST decompositions as our adopted distance. For galaxies in which we were limited to V(HST), we adopt the values that band predicts. We list the uncertainty on the best estimate distance as 20%, which is the typical uncertainty noted by CF1 and CF2 for TF-based distances. In cases where the uncertainty of the mean of all available TF distances for each galaxy is >20%, we list that value as the uncertainty. We have marked each galaxy with a quality flag for the distance based on comparison with literature, the mass distributions in the CF3 DVC, and peculiar velocities (see Section 4), a = best quality, b = moderate quality, c = poor quality.

[a] Adopted using the H I line width from Ho et al. (2008).

widths, following the formalism adopted for the other bandpasses. Our best-fit result is

$$M_V^{b,i,k} = (-20.39 \pm 0.03) - (7.62 \pm 0.15)(\log W_{\rm mx}^{i} - 2.5). \tag{19}$$

We find a negligible change to the final result if we instead employ the updated Galactic extinction values from Schlafly & Finkbeiner (2011). When substituted, the slope and intercept shift slightly to −7.59 and −20.36, respectively. The calibrated relationship for the V band sits between the existing calibrated relationships for the B and R bands, and also agrees well with the recent TF calibrations of Kourkchi et al. (2020) for SDSS bands, especially when compared to g and r.

5.3. Final Distances and Peculiar Velocities

To constrain the TF distances, we utilized the deprojected H I line widths and calibrated TF relationships to derive absolute

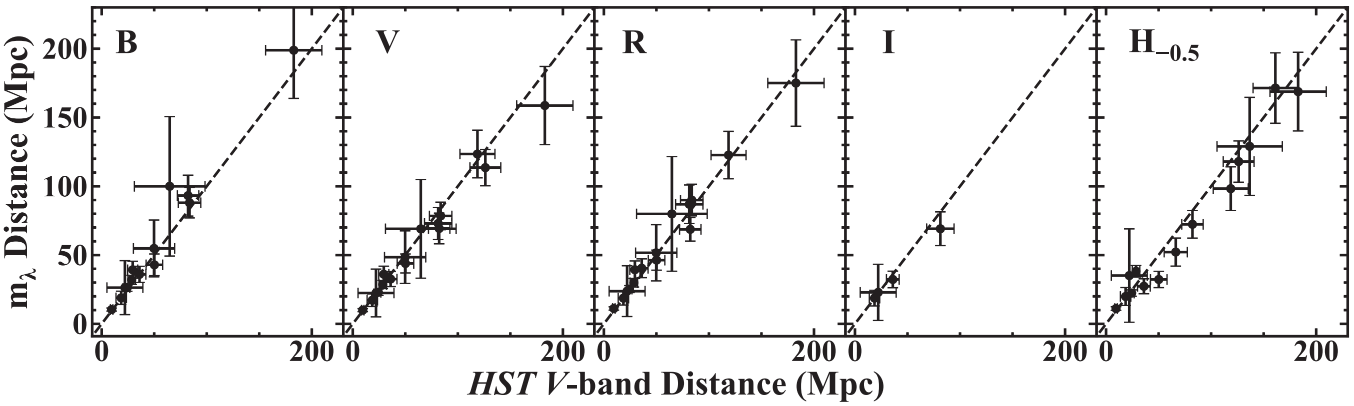

Figure 4. Comparisons between the TF distances determined by our calibration of the *V*-band relationship using our HST images to (from left to right) ground-based *B*-, *V*-, *R*-, *I*-, and $H_{-0.5}$-band distances. A line of unity is drawn in all panels. The error bars are the individual uncertainties of each distance calculation (see Table 5). We find good agreement for all calibrations within the uncertainties.

magnitudes for each galaxy in each available bandpass. We then calculated the distance moduli between our corrected apparent magnitudes and derived absolute magnitudes to constrain each distance. All corrected H I line widths and apparent magnitudes used in distance calculations are listed in Table 4, and the distance measurements for all bands are tabulated in Table 5.

In Figure 4, we compare the ground-based distances to the distances based on the *V*-band HST apparent magnitudes due to their superior spatial resolution and lack of seeing effects. Within the uncertainties, we generally find close agreement between the distances derived from the different photometric bands. In addition to the superior image quality of the HST data, the models of the ground-based images were guided by, and in some cases held fixed to, the parameters determined from the HST images. The axis ratios from the models of the HST images were used to derive the deprojected H I line widths in most cases, except for NGC 4051 and NGC 4593 as we described in Section 4.3. Therefore, we prefer the distances based on the photometry derived from the HST images and quote them as our adopted TF distances in Table 5. We adopt a typical uncertainty of 20%, as used by CF1 and CF2 for TF-based distances. However, the ground-based photometry, especially when multiple bandpasses were available, can provide some additional insight into the uncertainties, so we list the uncertainty of the weighted mean as the final adopted uncertainty in cases where it was larger than 20% of the distance (3/24 galaxies). Though we employ the updated Galactic extinction values of Schlafly & Finkbeiner (2011), the calibrations of Tully et al. (2008) and Tully & Courtois (2012) utilized the previous values of Schlegel et al. (1998). We find a negligible change to our final distances if we instead employ the Schlegel et al. (1998) values, with a median fractional change of 0.4% for all galaxies in our sample.

Peculiar velocities relative to the Hubble flow, or $V_{\rm PEC}$, can be calculated as a check on the reliability of the TF distances. Galaxies in the local universe are generally observed to have $V_{\rm PEC}$ values $\lesssim 500\ {\rm km\ s^{-1}}$ (Tully et al. 2008), therefore, larger values require additional scrutiny. We calculated the modified, cosmologically adjusted galaxy velocity $V_{\rm MOD}$, described in Tully et al. (2013, 2016) as

$$V_{\rm MOD} = cz[1 + 0.5(1 - q_0)z - (1/6) \times (1 - q_0 - 3q_0^2 + 1)z^2], \tag{20}$$

where z is the redshift with respect to the cosmic microwave background rest frame, $q_0 = 0.5(\Omega_{\rm M} - 2\Omega_\Lambda)$, $\Omega_{\rm M} = 0.27$, and $\Omega_\Lambda = 0.73$. This velocity includes relativistic corrections to the observed velocity assuming a ΛCDM cosmology, which are small for galaxies with $z < 0.1$, like our sample.

$V_{\rm PEC}$ is then calculated as

$$V_{\rm PEC} = V_{\rm MOD} - H_0 D, \tag{21}$$

where we adopt $H_0 = 74\ {\rm km\ s^{-1}\ Mpc^{-1}}$ (Riess et al. 2019), and D is the adopted distance to the galaxy in megaparsecs.

5.4. Notes on Individual Objects

The TF distances we have determined are the first redshift independent distances for many of the galaxies in our sample. However, in a select few cases there are previously measured distances with which we can compare our results, primarily by Cepheid and SBF methods, and second the Cosmicflows programs (CF1, CF2, CF3; Tully et al. 2008, 2013, 2016). Previous TF measurements have been reported for nine galaxies in our sample, mostly in the *B* band, yet none have taken into account the contamination of the predominantly blue AGN in the nucleus. As discussed in Section 3, the brightness contribution of an AGN can be significant and will bias the distance modulus toward smaller values, as we have found with the majority of TF distances discussed below. We have tabulated previous distance measurements with their respective methods in Table 6.

Mrk 1044: There are previously published distances for Mrk 1044 from the *J*-, *H*-, and *K*-band TF calibrations of Theureau et al. (2007) of 86.8 ± 18.4, 78.5 ± 17.0, and 68.5 ± 14.2 Mpc, respectively. We find a distance to Mrk 1044 of 81.3 ± 16.3 Mpc, which lies within the estimates of Theureau et al. (2007). Our surface brightness decomposition of the HST *V*-band image is mostly consistent with the decomposition of the same image from Wang et al. 2014, however, we find a larger exponential disk radius of 21.9″ compared to their value of 21.2″.

NGC 3227: NGC 3227 is interacting with its neighboring elliptical galaxy NGC 3226, which has an SBF distance measurement of 23.7 ± 2.6 Mpc from Tonry et al. 2001, with a slight correction from Blakeslee et al. 2010. NGC 3227 also has two previously reported *B*-band TF distance determinations: Bottinelli et al. 1984 reported a *B*-band distance of

Table 6
Previous Measurements

Target	Distance (Mpc)	Method	Ref
Mrk 1044	68.5 ± 14.2	TF *K* band	1
	78.5 ± 17.0	TF *H* band	1
	86.8 ± 18.4	TF *J* band	1
NGC 3227	15.2	TF *B* band	2
	20.6 ± 3.8	TF *B* band	3
	23.7 ± 2.6[a]	SBF	4
NGC 3783	38.5 ± 14.2	TF *B* band[b]	2
NGC 4051	8.8 ± 1.8	TF 3.6 μm	5
	11.0 ± 1.0	TF *B* band	6
	11.0 ± 2.0	TF *I* band	7
	11.7 ± 1.6	TF *B* band	8
	12.2 ± 2.0	CF2	9
	12.4 ± 2.3	TF *B* band	10
	12.6 ± 1.5	TF *B* band	3
	16.6 ± 0.3	Cepheids	11
	17.0 ± 3.1	TF *B* band	12
NGC 4151	3.9 ± 0.6	CF1	13
	4.5 ± 0.8	TF *B* band	10
	4.8 ± 1.0	TF *B* band	8
	5.0 ± 0.7	TF *B* band	3
	5.7 ± 1.2	TF *K* band	1
	6.4 ± 1.4	TF *H* band	1
	6.9 ± 1.5	TF *J* band	1
	15.8 ± 0.4	Cepheids	14
	16.6 ± 1.1	SN 2018aoq	15
	20.0 ± 1.6	SN 2018aoq	15
	20.3 ± 3.7	TF *B* band	11
NGC 4593	25.6 ± 5.30	TF *K* band	1
	26.2 ± 5.7	TF *H* band	1
	26.6 ± 5.6	TF *J* band	1
	39.5 ± 14.5	TF *B* band[b]	11
NGC 5548	34.0 ± 8.8	TF *B* band	3
NGC 6814	8.6 ± 2.7	TF *B* band	3
	21.65 ± 0.41	Cepheids	16
	22.8 ± 4.2	TF *B* band	11
NGC 7469	35.6	TF *B* band	3
	50.0 ± 10.4	TF *K* band	1
	55.3 ± 12.0	TF *H* band	1
	57.30 ± 2.11	SN 2008ec	17
	59.6 ± 12.7	TF *J* band	1
	59.70 ± 4.57	SN 2008ec	17
	66.40 ± 6.23	SN 2008ec	18

Notes. References are as follows: 1. Theureau et al. (2007), 2. Tully & Fisher (1988), 3. Bottinelli et al. (1984), 4. Tonry et al. (2001), 5. Sorce et al. (2014), 6. Tully et al. (2013), 7. Tully et al. (2016), 8. Bottinelli et al. (1985), 9. Tully et al. (2009), 10. de Vaucouleurs et al. (1981), 11. Yuan et al. (2020a), 12. Tully & Fisher (1988), 13. Tully et al. (2008), 14. Yuan et al. (2020b), 15. Tsvetkov et al. (2019), 16. Bentz et al. (2019), 17. Koshida et al. (2017), 18. Ganeshalingam et al. (2013).

[a] Distance to interacting companion, with correction from Blakeslee et al. (2010).

[b] Estimated distance using the diameter-H I line width method (see Section 5.4).

15.2 Mpc, and Tully & Fisher (1988) reported an updated *B*-band distance of 20.6 ± 3.8. We report a distance of 24.3 ± 4.9 Mpc, which shows good agreement with the SBF measurement to its companion. The removal of the AGN contamination decreases the galaxy's apparent magnitude and results in the determination of a larger distance than both of the previous *B*-band TF determinations.

NGC 3783: NGC 3783 has a previous *B*-band TF estimate of 38.5 ± 14.2 Mpc (Tully & Fisher 1988) based on the diameter-H I line width relation. We report a slightly larger distance of 49.8 ± 10.0 Mpc. However, NGC 3783 is one of the most highly inclined systems in our sample, with an axis ratio of 0.96. Near face-on systems cause large uncertainties in $W_{\rm mx}^{i}$, and consequently a large uncertainty in the distance.

NGC 4051: There are numerous TF distance estimates for NGC 4051 with a large span of values, the most accurate of which is the recent Cepheids measurement by Yuan et al. (2020a) of 16.6 ± 0.3 Mpc. Sorce et al. (2014) reported a 3.6 μm TF distance of 8.8 ± 1.8 Mpc. *B*-band TF determinations span the range of 11.0−17.0 Mpc (de Vaucouleurs et al. 1981; Bottinelli et al. 1984, 1985; Tully & Fisher 1988; Tully et al. 2009). Finally, CF3 reports an *I*-band measurement of 11.0 ± 2.0 Mpc. Our distance is 9.5 ± 1.9 Mpc, surprisingly smaller than the previous TF distances given the removal of AGN contamination. The original axis ratio used by CF1 (and subsequently by CF2 and CF3) for NGC 4051 is 0.66, which is slightly more face-on than our constrained axis ratio of 0.58 from the ground-based surface brightness modeling (see Section 4.3). The higher inclination used by CF1 would produce a larger deprojected H I line width and subsequently brighter absolute magnitude predicted by the TF relation, thus resulting in a slightly larger distance of 10.9 Mpc.

NGC 4151: NGC 4151 has been studied by numerous groups in an attempt to constrain its distance, finding values that range from 4.5–20.3 Mpc (de Vaucouleurs et al. 1981; Bottinelli et al. 1984, 1985; Tully & Fisher 1988). The most accurate distance comes from a recent Cepheid study, which found 15.8 ± 0.4 Mpc (Yuan et al. 2020b). Almost all of the TF studies underpredict the distance, which seems to be caused by the adoption of an axis ratio of 0.6 when constraining the galaxy inclination. Resolved H I imaging of NGC 4151 (Mundell et al. 1999) suggests a much more face-on orientation of $\sim 21^\circ$. Adopting this value constrains our TF estimate of the distance to 18.6 ± 3.7 Mpc, slightly larger than but consistent with the Cepheids distance.

NGC 4593: Theureau et al. (2007) measured *J*-, *H*-, and *K*-band TF distances to NGC 4593 of ∼26 Mpc, which agrees fairly well with our finding of 28.5 ± 5.7 Mpc. Tully & Fisher (1988) estimated a much larger distance of 39.5 ± 14.5 Mpc based on the H I line width–diameter TF relation. However, as shown originally by Tully & Fisher (1977) and noted by Bottinelli et al. (1983), the diameter relation is much less accurate than the luminosity–H I line width relationship.

NGC 5548: The previous *B*-band TF measurement from Bottinelli et al. (1984) places NGC 5548 at a distance of 34.0 ± 8.8 Mpc. We find a distance of 45.0 ± 3.8 Mpc with a large $V_{\rm PEC}$ of 2104 ± 288 km s^{-1}. However, the large predicted $V_{\rm PEC}$, in addition to the turbulent and low S/N H I profile, suggest this may not be a reliable distance. Ho et al. (2008) collected a higher S/N H I spectrum with $W_{20} = 321.1 \pm 6.8$ km s^{-1}. Using this measurement predicts $D = 83.6 \pm 16.7$ Mpc with a more reasonable $V_{\rm PEC} = -753 \pm 1242$ km s^{-1}. We therefore adopt this distance for NGC 5548 and list it in Table 5.

NGC 6814: Bentz et al. (2019) recently reported a Cepheid-based distance to NGC 6814 of 21.6 ± 0.4 Mpc. There are also *B*-band TF estimates that range from 8.6–22.8 Mpc (Bottinelli et al. 1984; Tully & Fisher 1988). Even though NGC 6814 is almost perfectly face-on (with an axis ratio of 0.98) and therefore has a large uncertainty, the TF distance we predict of 22.1 ± 8.0 Mpc is in good agreement with the Cepheids value.

NGC 7469: NGC 7469 was host to SN 2008ec, a Type Ia supernova. Analysis of the supernova light curve by Koshida et al. (2017) and Ganeshalingam et al. (2013) constrained distances of 57.30–66.40 Mpc. There are also multiple TF distance determinations to NGC 7469, including a *B*-band measurement of 35.6 Mpc (Bottinelli et al. 1984) and JHK measurements of 50.0–59.6 Mpc (Theureau et al. 2007). However, in our analysis of the H I spectrum in Paper I, we commented on possible flux contribution to the blueshifted flank of NGC 7469 from companion galaxy IC 5283. Higher S/N emission line detections in the literature most likely include the flux contribution of the companion (Mirabel & Wilson 1984; Mirabel & Sanders 1988; Ho et al. 2008), while our lower S/N profile does not share the same signature. We have tested distances predicted using the W_{20} measurements (with the W_R^i definition) from the literature to compare to our result. If 525.1 km s^{-1} from Ho et al. (2008) is used, we calculate 140 Mpc. If we use 395 km s^{-1} from Mirabel & Wilson (1984), the resulting distance is 91 Mpc. Using our width, our distance is 36.0 ± 7.2 Mpc with a $V_{\rm PEC}$ of 1949 ± 535 km s^{-1}. Due to the interaction of IC 5283 and uncertainty in the width of the emission line, resolved H I observations are necessary to both separate the interacting galaxies and improve on the current distance estimates which rely on the H I line width.

5.5. Selection of Final Adopted Distances

For all galaxies except Mrk 478, we are able to compare our distances to the distances predicted by the CF3 Distance-Velocity Calculator (CF3 DVC; Kourkchi et al. 2020) based on the velocity field from the Numerical Action Methods model (Shaya et al. 2017, $D < 38$ Mpc) and the Velocity and Density Field Model (Graziani et al. 2019, $D < 200$ Mpc). The CF3 DVC predicts a distance based on the Cosmicflows model of the local velocity field in a specific region of the sky. It also displays distances and velocities of known galaxy groups and clusters within the search region that define the local model, allowing us to analyze the density of matter in a particular region. The local gravitational interactions between a galaxy and its environment cause individual $V_{\rm PEC}$ values.

For Mrk 1044 ($V_{\rm PEC} = -1275 \pm 1212$), Ark 120 ($V_{\rm PEC} = -1855 \pm 2394$), SBS1116 + 583A ($V_{\rm PEC} = -1393 \pm 2030$), NGC 4748 ($V_{\rm PEC} = -1513 \pm 1219$), and Mrk 290 ($V_{\rm PEC} = -2644 \pm 2416$), the $V_{\rm PEC}$ values we calculate agree with the range of peculiar velocities observed by CF1 within the large uncertainties. The peculiar velocities of Mrk 6 ($V_{\rm PEC} = -3625 \pm 1873$), Mrk 79 ($V_{\rm PEC} = 3181 \pm 743$), and Mrk 1310 ($V_{\rm PEC} = -2480 \pm 1762$) are large, but still within those observed by the larger CF2 and CF3 catalogs (maximum observed $V_{\rm PEC}$ of ∼4000 km s^{-1}), and could be caused by the mass distributions near each galaxy's position on the sky present in the CF3 catalog. We confirmed that the CF3 DVC shows known, localized mass concentrations occupying distributions of either smaller or larger distances than those predicted by the DVC. These suggest local gravitational wells, and the resultant blueshifts or redshifts would cause each galaxy to appear closer or farther, assuming the recessional velocities are equivalent to the Hubble flow.

For MCG+08-11-011, Mrk 374, Mrk 817, Mrk 478, NGC 5940, and Zw 229-015, however, we are unable to further check our TF distances with the CF3 DVC results (mostly due to the lack of clusters present in the CF3 catalog near the position of each galaxy) or any literature results. Within the uncertainties, these $V_{\rm PEC}$ constraints are all >1000 km s^{-1}, which we set as the cutoff for galaxies in which we were unable to analyze the local mass distribution. The same is true even if we adopt the uncertainty typically considered by Tully et al. (2008) of 20%. Our estimated distance for Mrk 478 is 282.2 Mpc, which is beyond the 200 Mpc limit of the CF3 DVC. Additionally, as previously discussed, any distance measurement which relies on current H I line width measurements of NGC 7469 is suspect. Thus, we have deemed the TF distances to these seven galaxies as uncertain, and have assigned each with the poor quality flag "c" in Table 5.

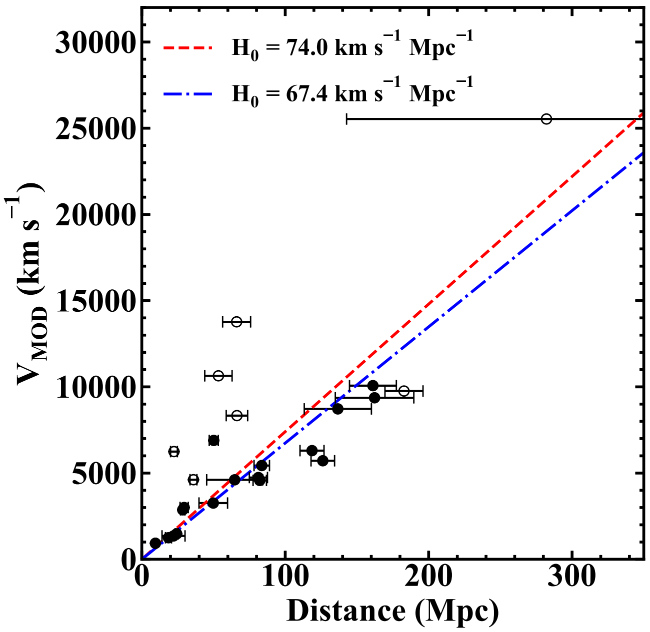

Figure 5. Hubble diagram exhibiting our TF distances vs. their cosmologically adjusted velocity $V_{\rm MOD}$. Points shown in open circles represent the seven TF distances we have deemed as uncertain (see Section 5.4), MCG+08-11-011, Mrk 374, Mrk 817, Mrk 478, NGC 5940, Zw 229-015, and NGC 7469. The closed points are our remaining, certain distance measurements. We compare these to the Hubble–Lemaître law, with H_0 values of 74.0 km s^{-1} Mpc^{-1} determined by Riess et al. (2019) and 67.4 km s^{-1} Mpc^{-1} determined by the Planck Collaboration et al. (2020).

We note that the galaxy inclinations of the majority of this sample lie below the usual limit of 45° for TF studies in the literature, namely, the Cosmicflows programs. Systems with tendencies toward face-on orientations cause large uncertainties in the deprojected H I line widths, and consequently, high uncertainties on distance and $V_{\rm PEC}$ constraints. We also note that the majority of the outliers in Figure 5 have TF distance measurements far too small for their $V_{\rm MOD}$ given the Hubble flow for either value of H_0 we have displayed. The TF relation is calibrated with inactive galaxies, thus it is of interest to explore potential differences between active and inactive galaxies that could cause discrepancies in the predicted distances for this sample of AGN hosts.

The analysis of color–magnitude diagrams for mass-matched samples of AGN and non-AGN hosts from the Chandra Deep Field North and South surveys by Xue et al. (2010) found that the star formation rates in active galaxies are typically a factor of ∼2–3 higher than quiescent galaxies for $0 < z < 1$. Increased star formation has been shown to lead to an increase in surface

Table 7
Final Adopted Distances and Mass Estimates

Target (1)	Distance (Mpc) (2)	Ref (3)	R_{HI} (Kpc) (4)	M_{BH} $(M_{\odot})$ (5)	M_{*} $(M_{\odot})$ (6)	M_{BARY} $(M_{\odot})$ (7)	M_{DYN} $(M_{\odot})$ (8)	M_{DM} $(M_{\odot})$ (9)
Mrk 1044	81.3 ± 16.3	1	8.10 ± 1.87	$6.71\ ^{+0.12}_{-0.10}$	10.02 ± 0.43	10.20 ± 0.32	10.71 ± 0.11	10.55 ± 0.22
Ark 120	161.2 ± 32.2	1	16.74 ± 4.39	$8.07\ ^{+0.05}_{-0.06}$	11.13 ± 0.22	11.18 ± 0.21	11.47 ± 0.11	11.15 ± 0.27
MCG+08-11-011	84.2 ± 6.9	2	39.45 ± 8.60	$7.43\ ^{+0.15}_{-0.15}$	11.10 ± 0.42	11.15 ± 0.39	11.47 ± 0.09	11.19 ± 0.38
Mrk 6	126.2 ± 25.2	1	30.63 ± 9.29	$8.10\ ^{+0.04}_{-0.04}$	11.05 ± 0.22	11.08 ± 0.21	11.76 ± 0.12	11.65 ± 0.16
Mrk 374	185.3 ± 7.0	2	41.08 ± 5.81	$7.30\ ^{+0.31}_{-0.31}$	10.84 ± 0.42	10.86 ± 0.41	11.32 ± 0.08	11.13 ± 0.28
Mrk 79	50.2 ± 10.0	1	13.10 ± 3.19	$7.61\ ^{+0.11}_{-0.14}$	10.13 ± 0.22	10.19 ± 0.20	10.72 ± 0.11	10.56 ± 0.17
NGC 2617	64.7 ± 19.5	1	12.70 ± 6.10	$7.49\ ^{+0.14}_{-0.14}$	10.54 ± 0.44	10.68 ± 0.36	11.17 ± 0.26	10.99 ± 0.37
NGC 3227	23.7 ± 2.6	3	17.89 ± 4.48	$6.77\ ^{+0.08}_{-0.11}$	11.04 ± 0.20	11.05 ± 0.20	11.32 ± 0.10	10.99 ± 0.27
SBS1116 + 583A	136.7 ± 27.3	1	11.23 ± 2.94	$6.56\ ^{+0.08}_{-0.09}$	10.48 ± 0.22	10.50 ± 0.22	10.77 ± 0.14	10.44 ± 0.32
NGC 3783	49.8 ± 10.0	1	23.98 ± 5.95	$7.37\ ^{+0.08}_{-0.08}$	11.08 ± 0.21	11.11 ± 0.20	11.51 ± 0.19	11.29 ± 0.30
Mrk 1310	118.7 ± 23.7	1	11.41 ± 2.78	$6.21\ ^{+0.07}_{-0.09}$	10.28 ± 0.22	10.38 ± 0.18	10.90 ± 0.11	10.75 ± 0.17
NGC 4051	16.6 ± 0.3	4	17.47 ± 1.94	$6.13\ ^{+0.12}_{-0.16}$	10.10 ± 0.19	10.19 ± 0.16	10.91 ± 0.06	10.82 ± 0.09
NGC 4151	15.8 ± 0.4	5	8.35 ± 1.13	$7.56\ ^{+0.05}_{-0.05}$	10.35 ± 0.19	10.41 ± 0.17	10.76 ± 0.13	10.50 ± 0.24
NGC 4593	28.5 ± 5.7	1	21.04 ± 6.45	$6.88\ ^{+0.08}_{-0.10}$	10.58 ± 0.22	10.60 ± 0.22	11.37 ± 0.12	11.29 ± 0.15
NGC 4748	82.2 ± 16.4	1	16.58 ± 5.21	$6.41\ ^{+0.11}_{-0.18}$	10.70 ± 0.22	10.73 ± 0.21	11.25 ± 0.12	11.09 ± 0.19
NGC 5548	83.6 ± 16.7	1	24.84 ± 5.96	$7.72\ ^{+0.02}_{-0.02}$	11.19 ± 0.22	11.20 ± 0.22	11.61 ± 0.10	11.40 ± 0.20
Mrk 817	130.8 ± 6.9	2	14.04 ± 2.74	$7.59\ ^{+0.06}_{-0.07}$	10.92 ± 0.19	10.93 ± 0.19	11.39 ± 0.10	11.21 ± 0.17
Mrk 478	342.7 ± 7.2	2	30.39 ± 4.19	$7.40\ ^{+0.18}_{-0.18}$	11.13 ± 0.42	11.17 ± 0.40	11.67 ± 0.22	11.51 ± 0.34
NGC 5940	141.6 ± 6.9	2	34.15 ± 4.94	$7.04\ ^{+0.07}_{-0.06}$	11.03 ± 0.29	11.07 ± 0.27	11.33 ± 0.10	10.98 ± 0.34
Mrk 290	162.3 ± 32.5	1	17.52 ± 4.24	$7.28\ ^{+0.06}_{-0.06}$	10.79 ± 0.30	10.81 ± 0.29	11.16 ± 0.12	10.90 ± 0.29
Zw 229-015	115.5 ± 6.9	2	28.16 ± 5.07	$6.91\ ^{+0.07}_{-0.12}$	10.26 ± 0.19	10.30 ± 0.18	10.95 ± 0.10	10.84 ± 0.13
1H1934-063	29.5 ± 5.9	1	5.57 ± 1.45	$6.40\ ^{+0.17}_{-0.20}$	10.15 ± 0.21	10.17 ± 0.21	10.42 ± 0.12	10.07 ± 0.31
NGC 6814	21.6 ± 0.4	6	11.91 ± 3.03	$7.04\ ^{+0.06}_{-0.06}$	10.33 ± 0.19	10.40 ± 0.16	11.02 ± 0.31	10.90 ± 0.38
NGC 7469	61.9 ± 3.3	7	17.06 ± 2.12	$6.96^{+0.05}_{-0.05}$	10.78 ± 0.19	10.81 ± 0.18	11.05 ± 0.09	10.67 ± 0.28

Note. Final adopted distances and mass estimates for the AGN hosts in this study. The reference for each adopted distance in Column 3 is as follows: 1. TF distance; this work, 2. Redshift-based distances consistent with those reported in Paper I, adjusted for $H_0 = 74$ km s^{-1}, 3. SBF estimate to interacting companion NGC 3226 (Tonry et al. 2001), 4. Cepheids measurement (Yuan et al. 2020a), 5. Cepheids measurement (Yuan et al. 2020b), 6. Cepheids measurement (Bentz et al. 2019), 7. Average SN1a distance (Koshida et al. 2017; Ganeshalingam et al. 2013). The majority of black hole masses are from the RM database of Bentz & Katz (2015) (see Section 6.2). The calculations for M_{BARY} are detailed in Paper I, and M_{DYN} and M_{DM} are described in Section 6.

brightness (e.g., Graves & Faber 2010; Mould 2020), and a higher surface brightness would lead to a brighter apparent magnitude, thus causing a galaxy to appear closer than it is. Additionally, in their study of the *R*-band TF relation for close galaxy pairs, Barton et al. (2001) found that triggered star formation is a significant contributor to the difference in slope from the TF relation. Whether higher star formation rates are caused by AGN activity or interactions, the observational effect would be consistent in that the galaxy would appear brighter than a comparable inactive or isolated galaxy, leading to a distance estimate that is biased low. Active galaxies might therefore be reasonably expected to show a larger scatter about the canonical TF relation.

All final TF distances are shown in the Hubble diagram in Figure 5, where the aforementioned uncertain distances are open circles, and the rest are closed circles. For the remainder of this work, we apply the redshift-based distances for MCG +08-11-011, Mrk 374, Mrk 817, Mrk 478, NGC 5940, and Zw 229-015, consistent with those reported in Paper I. We employ the SBF distance to NGC 3226 as the adopted distance to NGC 3227 (Tonry et al. 2001; Blakeslee et al. 2010), the Cepheid distance measurements to NGC 4051, NGC 4151, and NGC 6814 (Yuan et al. 2020a, 2020b; Bentz et al. 2019), and the average of the SN1a distances to NGC 7469 (Ganeshalingam et al. 2013; Koshida et al. 2017). Final adopted distances are tabulated in Table 7.

6. Masses

With distances and physical surface brightness details constrained, we are able to estimate the masses of the AGN hosts in our sample and explore their relationships to the central SMBH masses. Here we detail the methods of measurement for dynamical mass (M_{DYN}) and dark matter mass (M_{DM}) and adopted measurements of M_{BH}.

6.1. Dynamical and Dark Matter Mass

Measurement of the maximum rotation rate (V_{mx}) of a disk galaxy allows the total enclosed mass of the system, or M_{DYN}, to be measured. H I is one of the best tracers of galaxy rotational velocity at the outer extents of the disk, as its distribution usually extends much farther than the high surface brightness stellar component (i.e., Walter et al. 2008; Ott et al. 2012; Koribalski et al. 2018). V_{mx} is most precisely measured from the flat portion of H I rotation curves (i.e., de Blok et al. 2008), however, the unresolved H I emission line is more commonly used as it requires far fewer observational resources to acquire.

The large-scale velocity dispersion of H I is negligible, ~10 km s^{-1}, (Tamburro et al. 2009; Ianjamasimanana et al. 2012) relative to the rotational velocity. The broadening of the emission line is thus dominated by virial rotation, and the virial theorem describes the mass enclosed in the system as

$M_{\rm DYN} = (RV^2_{\rm mx})/{\rm G}$, where R is a characteristic radius and G is the gravitational constant. In our case, R is the radial extent of the H I distribution, and $V_{\rm mx}$ is equivalent to $W^i_{\rm mx}/2$, as Tully & Fouque 1985 have shown $W_{\rm mx}$ to be statistically equal to twice the maximum rotation rate.

There are multiple ways of estimating the H I radius in the literature. In their 21 cm study of 108 spiral galaxies, Broeils & Rhee (1997) found a relation between the H I radius and R_{25}. For galaxies where we have B-band images, we therefore adopt their relation of $R_{\rm HI} = (1.70 \pm 0.16)R_{25}$ with our R_{25} measurements from B-band isophote analyses (see Section 5). In the cases where B-band data are unavailable for the sample (Ark 120, Mrk 374, SBS1116+583A, Mrk 478, NGC 5940, Mrk 290, Zw 229-015), we look to the collection of template disk galaxy rotation curves by Catinella et al. (2006) and de Blok & Walter (2014), and use the relation $R_{25} = 3.2\ R_d$, with the R_d measurements listed in Table 2. Combining these definitions yields $R_{\rm HI} = (5.4 \pm 0.5)\ R_d$, which agrees with the H I rotation curve analysis of de Blok & Walter (2014) that shows the maximum extent of all curves to be $\sim 5\ R_d$. Therefore, for the remainder of the sample that do not have B-band data, we adopt $R_{\rm HI} = (5.4 \pm 0.5)\ R_d$.

Additionally, Wang et al. (2016) recalibrated the relation between the diameter of the H I disk and H I mass, resulting in an extremely tight relationship over 5 orders of magnitude in mass. With this calibrated relationship, the integrated 21 cm H I flux measurement may be employed to estimate $R_{\rm HI}$, as opposed to relying on the assumption of uniform scaling between the H I and optical sizes for all morphological types. We find a median fractional decrease of ∼18% in $R_{\rm HI}$ with this method compared to our adopted method of estimating $R_{\rm HI}$, which is within our typical uncertainty of ∼24%.

A recent study by Trujillo et al. (2020) sought to derive a physically motivated galaxy radius definition. Such a radius would correspond to a clearly measurable galaxy property, and they suggest the radius at which the star formation threshold is reached (R_1). The gas density for this threshold is usually estimated to be ~ 3–$10\ M_\odot\ {\rm pc}^{-2}$ for gas-to-star transformation efficiencies of ∼100% (Schaye 2004). However, Trujillo et al. 2020 argued that if the efficiency is less than 100%, a more reasonable estimation is $1\ M_\odot\ {\rm pc}^{-2}$, which corresponds to an efficiency of ∼10%. H I has been observed to condense to molecular hydrogen at a threshold of $\sim 10\ M_\odot\ {\rm pc}^{-2}$ (Martin & Kennicutt 2001; Wong & Blitz 2002; Bigiel et al. 2008), and molecular clouds are the typical locations of star formation (e.g., Leroy et al. 2008). H I surface density should therefore be linked to star formation, and Trujillo et al. suggested that R_1 could be closely related to $R_{\rm HI}$. To investigate this, we follow the prescriptions of Trujillo et al. (2020), which were derived from SDSS colors and a Chabrier initial mass function (Chabrier 2003), to transform the surface brightness profiles of the galaxies in our sample to stellar mass densities, and measure radii at $1\ M_\odot\ {\rm pc}^{-2}$. When compared to our $R_{\rm HI}$ estimates, we find an average ratio of $R_{\rm HI}$ to R_1 of ∼1.1, supporting the similarity between the two. We display the comparison between the two measurements in Figure 6. While we do not employ this method to estimate $R_{\rm HI}$, and while our sample is somewhat small and we employ estimates rather than measurements of $R_{\rm HI}$, the agreement between R_1 and $R_{\rm HI}$ may suggest a promising new avenue for constraining $R_{\rm HI}$ without resolved H I studies.

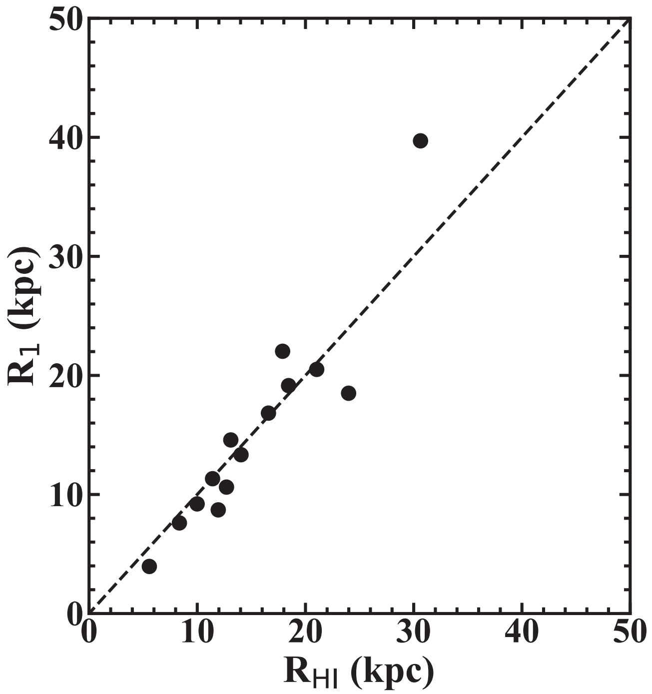

Figure 6. Comparison between $R_{\rm HI}$ and the radius at which the stellar mass density reaches $1\ M_\odot\ {\rm pc}^{-2}$, R_1, a proxy for the star formation threshold. We have followed the prescriptions from Trujillo et al. (2020) to convert the B-band surface brightness profiles of the galaxies in our sample to mass density profiles (see Section 6), after which R_1 was able to be measured. A line of unity is drawn, and we find good agreement between the two radii, with an average fraction of $R_{\rm HI}/R_1 \sim 1.1$.

With $R_{\rm HI}$ estimates for all galaxies in our sample, the total enclosed mass $M_{\rm DYN}$ is calculated by

$$M_{\rm DYN} = \left(\frac{R_{HI}(W^i_{\rm mx}/2)^2}{G}\right), \tag{22}$$

with $R_{\rm HI}$ in units of kiloparsecs translated from the angular disk sizes by our adopted distances. The constraint on the amount of dark matter, then, is simply the difference between the total enclosed mass and luminous mass, $M_{\rm BARY}$, calculated as

$$M_{\rm DM} = M_{\rm DYN} - M_{\rm BARY}, \tag{23}$$

where our $M_{\rm BARY}$ values are the sum of the gas mass and the stellar mass (M_*), or $M_{\rm BARY} = 1.4\ M_{\rm HI} + M_*$. The factor of 1.4 on $M_{\rm HI}$ accounts for the contribution of helium. H I masses are adopted from Paper I, and the stellar masses are adopted from Bentz & Manne-Nicholas (2018) with a few additions in Paper I, both of which have been updated with our final adopted distances reported in this work. M_*, $M_{\rm BARY}$, $M_{\rm DYN}$, and $M_{\rm DM}$ are reported in Table 7.

6.2. Black Hole Mass

All of the galaxies in this work belong to the sample of AGNs with direct black hole mass measurements from RM (Blandford & McKee 1982; Peterson 1993). RM measures the echo between the continuum variations of the nucleus, likely arising from the accretion disk, and the response of optically thick gas in the BLR moving at Doppler velocities. The time delay (τ) in the BLR variations is due to the extra path length traveled by the ionizing photons, and provides a measurement of the radius of the BLR ($R_{\rm BLR}$). When $R_{\rm BLR}$ is combined with the Doppler-broadened emission line width via the virial theorem, a constraint on the enclosed mass is obtained, the majority of which is due to the SMBH. The mass is given by

$$M_{\rm BH} = f\frac{c\tau V^2}{\rm G}, \quad (24)$$

where $c\tau$ is the effective radius, V is the width of the broad emission line, G is the gravitational constant, and f is an order of unity scale factor accounting for the unknown geometry and kinematics of the unresolved BLR. We adopt $\langle f \rangle = 4.3$ (Grier et al. 2013).

The majority of $M_{\rm BH}$ values are adopted from the AGN Black Hole Mass Database (Bentz & Katz 2015), and are the same as those used in our analysis in Paper I. For MCG+08-11-011, Mrk 374, and NGC 2617, we utilized the virial $M_{\rm BH}$ from Fausnaugh et al. (2017) and scaled them with $\langle f \rangle = 4.3$. For Mrk 1044, we used the Hβ time delay from Hu et al. (2015) and the rms Hβ line width from Du et al. 2016 with our adopted $\langle f \rangle$ to arrive at an $M_{\rm BH}$ estimate. For NGC 5940, we adopt the rms line width from Barth et al. (2015) and time delay from Barth et al. (2013) to estimate $M_{\rm BH}$. Lastly, the black hole masses for Mrk 478 and 1H1934-063 are based on current work on in-hand RM data (G. de Rosa 2020, private communication; M. C. Bentz et al. 2020, in preparation). All $M_{\rm BH}$ values are listed in Table 7.

7. Discussion

With distances and derived masses in hand, we are able to place both in the context of other established and well-studied relationships. We first explore the most recent calibration of the Baryonic Tully–Fisher (BTF) relation (McGaugh et al. 2000), which can also be inverted to predict distance. Several scaling relations between $M_{\rm BH}$ and host-galaxy characteristics have also been explored in the literature, and in the past two decades have strongly suggested a co-evolving relationship between black holes and their host galaxies. Such examples include the $M_{\rm BH}$–$\sigma_\star$ relation (Ferrarese & Merritt 2000; Gebhardt et al. 2000; Kormendy & Ho 2013), the $M_{\rm BH}$–$L_{\rm BULGE}$ relation (Kormendy & Richstone 1995; Kormendy & Ho 2013), and the $M_{\rm BH}$–M_* relation (Bentz & Manne-Nicholas 2018), many of which are utilized as inputs to large cosmological simulations of galaxy evolution (e.g., Steinborn et al. 2015; Volonteri et al. 2016; Mutlu-Pakdil et al. 2018). Here, we investigate relationships between $M_{\rm BH}$ and $M_{\rm DYN}$, $M_{\rm DM}$ and galaxy halo mass ($M_{\rm HALO}$).

Linear regressions were carried out with LINMIX_ERR (Kelly 2007), which is a Bayesian-based fitting algorithm that includes uncertainties in both variables in addition to a random scatter component. The slopes, intercepts, and scatter we report for each relationship are the medians of the respective large, random draws from the posterior probability distributions. The uncertainties are the 1σ deviations of each distribution.

7.1. The Baryonic TF Relation

The past two decades have revealed that the most fundamental form of the TF relation is the BTF relation, which shows a tightly correlated linear relation between rotational velocity and total baryonic mass over 5 decades of mass (McGaugh et al. 2000; McGaugh 2005; Lelli et al. 2015; Iorio et al. 2017). The mass contribution of gas in massive galaxies is small, therefore, the BTF relation is equivalent to the classic TF relation on the high mass end. As calculations of both gas and stellar masses, which constitute $M_{\rm BARY}$, rely on distance, it is therefore of interest to compare our distances to those predicted by the BTF relation. Though some deviations from the relation have been observed, such as H I massive galaxies ($M_{\rm HI} \gtrsim 10^{10} M_\odot$; Courtois et al. 2015) and H I-rich ultra-diffuse galaxies (Mancera Piña et al. 2019), the distances predicted by the BTF relation here are expected to be largely similar to those predicted by the TF relation, as the typical gas-to-stellar mass fraction for this sample is ~13%. However, discrepancies may surface for a few galaxies with higher gas-to-stellar mass fractions (e.g., Mrk 1044, NGC 2617, Mrk 1310, Ark 120).

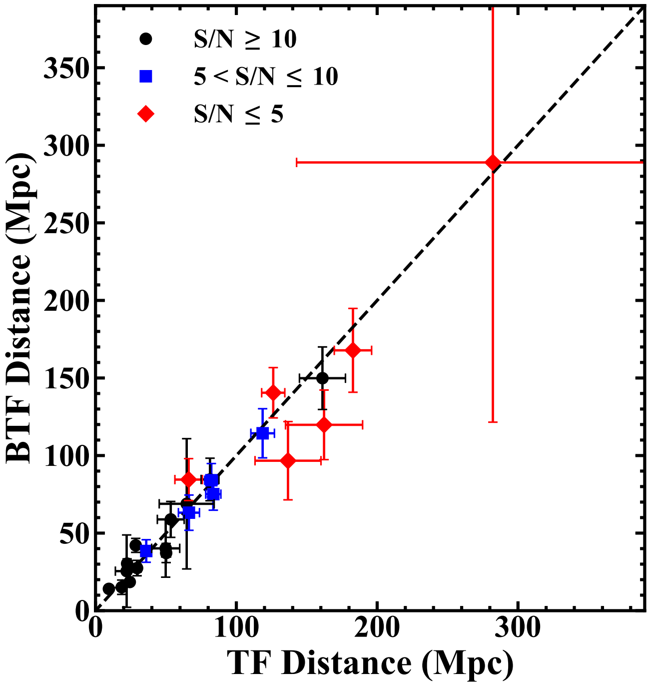

Figure 7. Comparison of our adopted distances (see Section 5.4) to those predicted by the BTF relation, using the W_{m50} calibration from Lelli et al. (2019). A line of unity is drawn. We display 3 H I emission line S/N thresholds (see Section 7.1), where black circles are ⩾10, blue squares are >5 and ⩽10, and red diamonds are ⩽5, which may relate to the source of discrepancy for the few outliers.

The BTF relation has been recently calibrated for several different definitions of rotational velocity measurement. We employ the calibration for our adopted velocity definition of W_{m50} from Lelli et al. 2019, which has a slope of 3.62 ± 0.09 and an intercept of 2.33 ± 0.20. This agrees well with the examination of the BTF relation by Zaritsky et al. (2014) using the Spitzer Survey of Stellar Structure in Galaxies (Sheth et al. 2010), which found a slope of 3.5 ± 0.2. We employ the H I fluxes given in Table 3 for the H I mass estimates, with the scaling factor to convert H I mass to total gas mass of 1.33 for consistency with the BTF definition. We note that we use a scale factor of 1.33 here, rather than the value of 1.4 that we employ throughout the rest of this work, only to ensure that we calculate values in the same way as they were calculated in the calibration of the relation. Additionally, we note that the BTF relation employs the smaller scale factor of 1.33 as the helium contribution (which the scale factor accounts for) is assumed to be lower for the H I-rich calibrating sample of the BTF relation (McGaugh 2012 and references therein). We use the stellar mass-to-light ratios of Bell & de Jong (2001) to estimate M_*. A comparison between the BTF distances and TF distances is shown in Figure 7. A line of unity is drawn, and we find

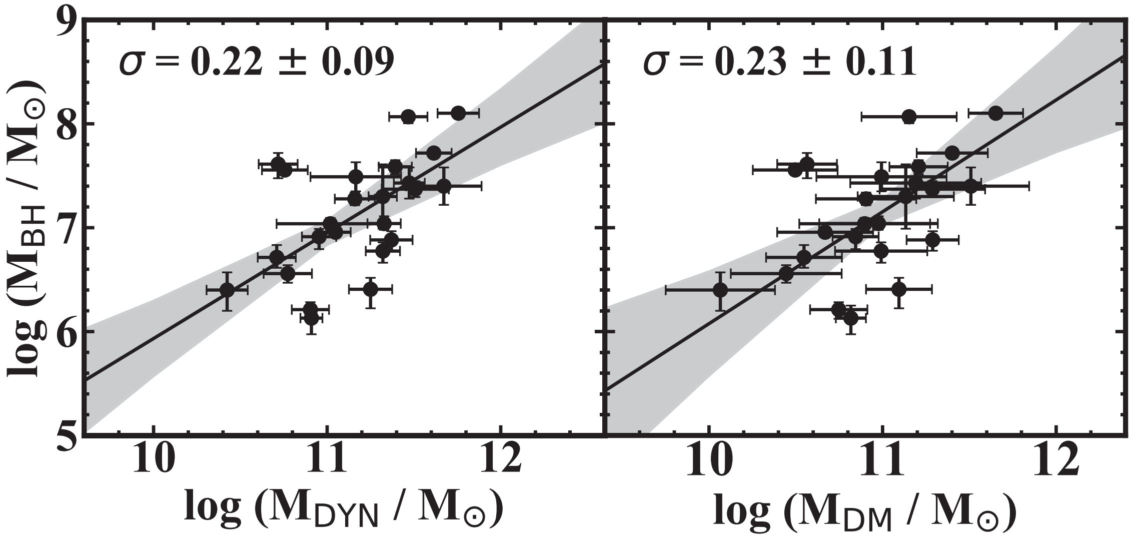

Figure 8. $M_{\rm BH}$ as a function of $M_{\rm DYN}$ (left) and $M_{\rm DM}$ (right). The best fits are displayed as solid, black lines in both panels. Uncertainties on the fits are displayed with gray shading around the best-fit lines. $M_{\rm DYN}$ values are calculated using $W^i_{\rm mx}/2$ as the maximum rotation rate and $R_{\rm HI}$ as the enclosing radius. $M_{\rm DM}$ is calculated as $M_{\rm DYN}{-}M_{\rm BARY}$. $M_{\rm BARY}$ values were updated from those calculated in Paper I with the adopted distances in this work (see Section 6).

generally good agreement between the TF distances and those predicted by the BTF relation.

The points in Figure 7 are labeled by H I emission line S/N, where profiles of $S/N \geqslant 10$ are black circles, $5 < S/N \leqslant 10$ are blue squares, and $S/N \leqslant 5$ are red diamonds. Mrk 290 and SBS1116 + 583A lie below the unity line, along with Ark 120 and Mrk 817, which lie below the line but agree within the uncertainties. The H I emission lines of these outliers all have a $S/N < 5$, which could result in underpredicting the flux and may be related to the cause of the discrepancies.

7.2. Dynamical Mass–Black Hole Mass and Dark Matter Mass–Black Hole Mass Relations

As described in Section 6, we utilize $R_{\rm HI}$ as the enclosing radius to estimate $M_{\rm DYN}$ for the galaxies in this sample. Here, we have examined the relationship between black hole mass and the total mass enclosed within the H I radius. The left panel of Figure 8 displays a clear trend between $M_{\rm BH}$ and $M_{\rm DYN}$, with the best fit given by

$$\log \frac{M_{\rm BH}}{M_\odot} = (1.02 \pm 0.35)\log\left(\frac{M_{\rm DYN}}{10^{12}M_\odot}\right) + (6.95 \pm 0.12), \tag{25}$$

with a scatter of (0.22 ± 0.09).

Using the difference between the total enclosed mass and the luminous mass, we have also explored the relationship between $M_{\rm BH}$ and dark matter mass. We plot $M_{\rm BH}$ versus $M_{\rm DM}$ in the right panel of Figure 8 and find a weaker, but still significant, correlation. The best fit to the relation is given by

$$\log \frac{M_{\rm BH}}{M_\odot} = (1.08 \pm 0.49)\log\left(\frac{M_{\rm DM}}{10^{12}M_\odot}\right) + (7.15 \pm 0.12), \tag{26}$$

with a scatter of (0.23 ± 0.11).

The average $M_{\rm DM}/M_{\rm DYN}$ fraction is $62 \pm 12\%$. However, we note that we are relying on the extent of the H I disk to measure $M_{\rm DYN}$ (and consequently $M_{\rm DM}$). The dark matter halo (DMH) is known to extend far beyond the visible radius, and thus we are probing only a fraction of the mass associated with each galaxy.

7.3. Halo Mass–Black Hole Mass Relation

We have also attempted to estimate the total enclosed mass within the halo radius, or $M_{\rm HALO}$. This includes estimates of the halo radius in relation to the H I radius and assumptions of the disk velocity at the halo radius ($V_{\rm HALO}$).

Kravtsov (2013) conducted a study relating R_{200} to several galaxy radius definitions. R_{200} is commonly treated as the radius of the DMH, and is the radius which encloses 200 times the critical density of the universe ($\rho_{\rm CR}(z)$). Halo radius hereafter is assumed to be equivalent to R_{200}. Through abundance matching of halo mass functions (Tinker et al. 2008; Klypin et al. 2011) and stellar mass functions (Bernardi et al. 2010; Papastergis et al. 2012), they first defined a relationship between stellar mass and the halo mass enclosed within R_{200}, or M_{200}. M_{200} was then estimated from $M_\star - M_{200}$ for a sample of galaxies with measured stellar masses that span 8 decades in M_* and all morphological types (Misgeld & Hilker (2011); Leroy et al. (2008); Zhang et al. (2012)). R_{200} was then estimated from M_{200}, where $M_{200} = (4\pi/3)200\rho_{\rm CR}(z)R^3_{200}$. Kravtsov 2013 found $R_{25} = 0.048\ R_{200}$, which when combined with $R_{\rm HI} = (1.70 \pm 0.16)\ R_{25}$ (Broeils & Rhee 1997) yields $R_{200} \sim (12.3 \pm 1.2)\ R_{\rm HI}$.

Additionally, Lapi et al. (2018) derived global galaxy properties such as M_{200} and R_{200} for a sample of 546 nearby late-type galaxies (Persic & Salucci 1995) by constructing templates of the rotation curve compilations of Persic et al. (1996), Catinella et al. (2006), and Yegorova et al. (2011). Templates were derived as a function of I-band luminosity. By modeling a DMH profile (Burkert 1995), R_{200} was derived by extrapolating the rotation curve to where the halo density reached $\rho_{\rm CR}(z)$. They then explored the relation between R_{200} and the effective galaxy stellar radius R_e (assumed to be equivalent to 1.68 R_d). While they quoted a polynomial form for the relationship, it is nearly linear within the sizeable scatter, except for a break in the trend toward smaller R_{200} at $R_e \sim 4$ kpc. Their best fit (approximated using solely the linear component) is $\log R_e = 0.73 \log R_{200} - 0.91$, which yields $R_{200} \sim (31.1 \pm 1.6)$ R_e. Using their formula $R_e \sim 1.68$ R_d and the relation $R_{\mathrm{HI}} \sim (5.4 \pm 0.5)$ R_d (Catinella et al. 2006; de Blok & Walter 2014) yields $R_{200} \sim (9.7 \pm 1.0)$ R_{HI}. Given the numerous approximations in both studies, we adopt $R_{200} \sim (11 \pm 1)$ R_{HI}, the average of the results of Kravtsov (2013) and Lapi et al. (2018).

In regards to V_{HALO}, if the DMH is assumed to have a constant density profile, it follows that the rotation curve would be flat out to R_{200}, thus, $V_{\mathrm{HALO}} \sim W^i_{\mathrm{mx}}/2$. This assumption is also adopted in the first derivation of a M_{BH}–M_{HALO} relation by Ferrarese (2002). Though for any density profile other than a constant, the disk circular velocity would decrease out to R_{200}, in which case $W^i_{\mathrm{mx}}/2$ would be an upper limit to V_{HALO} (as noted by Ferrarese 2002). The effect of the concentration parameter (the ratio of R_{200} to a characteristic inner radius) of the DMH on disk circular velocity was explored in the ΛCDM simulation of Bullock et al. (2001). The median of concentration parameters in the simulation showed an approximately flat rotation curve out to ~40 kpc. Additionally, The H I Nearby Galaxy Survey (Walter et al. 2008) measured flat rotation curves out to a maximum of ~50 kpc, compared to the median R_{200} estimate of Lapi et al. (2018) of ~150 kpc. Therefore, we assume a flat rotation curve out to R_{200}, and as follows $V_{\mathrm{HALO}} \sim W^i_{\mathrm{mx}}/2$.

We thus calculate the total enclosed mass M_{HALO} with the same formalism used to estimate M_{DYN}. In Figure 9 we explore the relationship between M_{BH} and M_{HALO}. The best fit, which is displayed with the solid line, is

$$\log \frac{M_{\mathrm{BH}}}{M_\odot} = (1.07 \pm 0.37) \log\left(\frac{M_{\mathrm{HALO}}}{10^{13} M_\odot}\right) + (7.97 \pm 0.31), \tag{27}$$

with a scatter of (0.22 ± 0.10) dex. The average fraction of dark matter within R_{200} is 97 ± 1%. The typical $M_{\mathrm{BH}}/M_{\mathrm{HALO}}$ fraction is 10^{-5}, but shows a trend with less massive black holes making up a smaller fraction of the total mass of the system, similar to what was found for $M_{\mathrm{BH}}/M_\star$ by Bentz & Manne-Nicholas (2018).

To place the M_{HALO} estimates in context with other methods used to derive total enclosed galaxy mass, we first compare to the M_{HALO} estimates used to construct the globular cluster system mass–galaxy halo mass relation (Spitler & Forbes 2009). In that study, halo masses were estimated using $M_\star$– M_{HALO} relations from weak gravitational lensing results (Hoekstra et al. 2005; Mandelbaum et al. 2006). The majority of the M_{HALO} estimates found by Spitler & Forbes (2009) fell within the range of $\sim 10^{10}$–10^{13} $M_\odot$ for a sample consisting of dE-, E-, S0-, and S-type galaxies. Additionally, the E-MOSAICS simulation (Bastian et al. 2020) of the globular cluster system mass–galaxy halo mass relation found that the majority of M_{HALO} constraints ranged from $\sim 10^{11}$–10^{13} $M_\odot$. Comparatively, our sample of halo estimates span the right orders of magnitude for galaxies of similar morphological type.

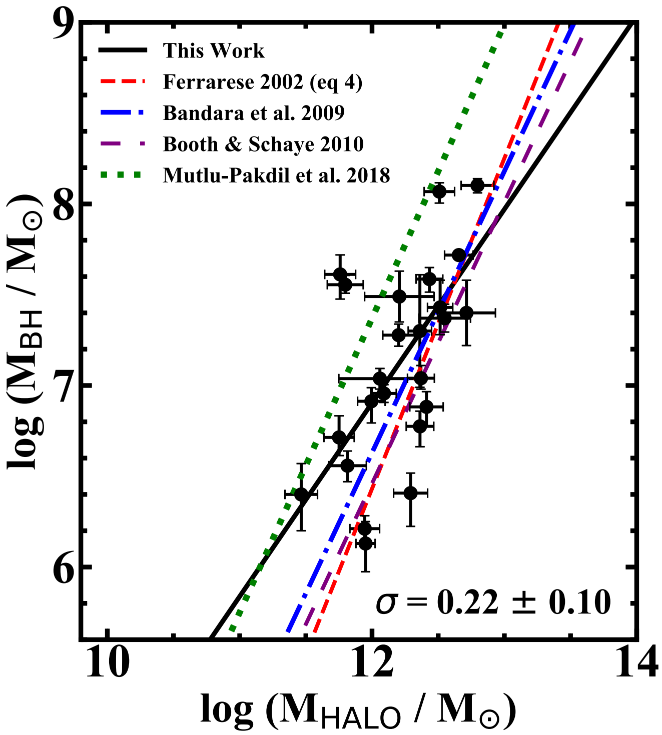

Figure 9. M_{BH} vs. estimates of M_{HALO}. We first use the average results of the relationships between observed radii and halo radii from Kravtsov (2013) and Lapi et al. (2018) to scale the R_{HI} values by (11 ± 1) to estimate R_{200}. We then assume a flat rotation curve out to R_{200} ($V_{\mathrm{HALO}} \sim W^i_{\mathrm{mx}}/2$) to arrive at an approximation of M_{HALO}. The solid black line is the formal fit to the data. The red dashed line is the first result from Ferrarese (2002), using the same assumption of a flat rotation curve. The blue dotted–dashed line is the relationship of M_{BH} to total gravitational mass from Bandara et al. (2009), which utilized gravitational lens modeling to constrain M_{HALO}. The purple dashed spaced line and green dotted line are the M_{BH}–M_{HALO} relations from the simulations of Booth & Schaye (2010) and Mutlu-Pakdil et al. (2018), respectively.

We have compared our fit to several other estimates of the M_{BH}–M_{HALO} relation. Ferrarese (2002) utilized $\sigma_\star$ measurements with the M_{BH}–$\sigma_\star$ relation to constrain SMBH masses that spanned $\sim 10^6$–10^9 $M_\odot$, along with several methods of estimating total gravitational mass, which fell within the range of $\sim 10^{11}$–10^{14} $M_\odot$. We plot the first derivation (Equation (4) in Ferrarese 2002), which assumes $V_{\mathrm{HALO}} \sim W^i_{\mathrm{mx}}/2$, as the red dashed line in Figure 9. We find a shallower slope than Ferrarese (2002), even if we refit their relationship with their sample restricted to the same mass ranges we find. However, we employ direct measurements of M_{BH}, while those in Ferrarese (2002) were estimated from the M_{BH}–$\sigma_\star$ relation. Additionally, we constrain W^i_{mx} from unresolved H I line widths, while Ferrarese 2002 utilized V_{mx} measurements from rotation curves. The differences in both measurements are potential sources of discrepancy in the M_{BH}–M_{HALO} relations. Ferrarese 2002 described two other methods of estimating M_{HALO}, however, both assume nonconstant halo density profiles, and as such predict less massive DMHs and intercepts ~0.5 dex and ~1.5 dex smaller than what we find, respectively.

We also compare to the observationally constrained relation from Bandara et al. (2009). Their M_{BH} values were derived using $\sigma_\star$ measurements and the M_{BH}–$\sigma_\star$ relation, and total galaxy mass was estimated from strong gravitational lens modeling (Bolton et al. 2008). We plot their relation as the blue dotted–dashed line in Figure 9. We again find a slightly shallower slope in comparison (though the fits of our relation and Bandara et al. 2009 are statistically equivalent within the uncertainties). However, their study probes only the high mass end of both black hole and halo mass, with their sample spanning $\sim 10^8 - 10^9$ $M_\odot$ in $M_{\rm BH}$ and $\sim 10^{13} - 10^{14}$ $M_\odot$ in $M_{\rm HALO}$.

Lastly, we have compared our results to those of large, hydrodynamical simulations. Booth & Schaye (2010) explored correlations between $M_{\rm BH}$–$M_\star$ and $M_{\rm BH}$–$M_{\rm HALO}$, which they defined as the mass enclosed within a sphere of a mean density of $200\rho_{\rm CR}(z)$. Their result is plotted as the purple dashed spaced line in Figure 9. The Illustris simulation also explored $M_{\rm BH}$–$M_{\rm HALO}$ (where the definition of $M_{\rm HALO}$ is the same as that of Booth & Schaye 2010), and we plot the result of Mutlu-Pakdil et al. (2018) as the green dotted line. The intercepts of their relations differ by a decade, most likely due to the difference in DMH density profiles between the simulations. Pillepich et al. (2014) reported that the halo density profile for the Illustris galaxies is well characterized by a negative power law, which would result in less massive haloes due to the quicker drop-off in density. Interestingly, galaxies in the the upgraded IllustrisTNG simulation (Lovell et al. 2018, which incorporated a larger volume, higher resolution, and new physics such as black hole-driven winds) are a much better match to observations, with flat rotation curves out to large radii ($\sim$60 kpc for $M_{200} = 10^{13}$ $M_\odot$). While the $M_{\rm BH}$–$M_{\rm HALO}$ relationship has not yet been reexamined for IllustrisTNG, the flatter rotation curves will result in a larger enclosed mass within R_{200} and may provide a better match to observationally constrained relationships such as the one we present here.

8. Summary

We presented TF distance measurements for 24 AGN host galaxies with direct $M_{\rm BH}$ measurements from RM. We also presented the first calibration of the *V*-band TF relation. These are the first redshift independent distance determinations for 14 active galaxies. We utilized HST *V* band and ground-based *B*-, *V*-, *R*-, *I*-, and *H*-band images to constrain multiple distance measurements for 19 galaxies. Removal of the bright nucleus via surface brightness modeling has allowed measurements of the distance moduli free of AGN contamination for the first time. Generally close agreement was found between distances derived from different photometric bandpasses within the uncertainties, and we found good agreement between the TF distances and those predicted by the BTF relation.

We collected available distance measurements from Cepheids (NGC 4051, NGC 4151, NGC 6814), SBF (NGC 3227), and SN1a (NGC 7469), *z*-based distances for 6 galaxies for which we deem the TF distances as uncertain (MCG+08-11-011, Mrk 374, Mrk 817, Mrk 478, NGC 5940, Zw 229-015), and the remaining 13 TF distances for estimates of galaxy dynamical and dark matter masses. We combined these with $W^i_{\rm mx}/2$ and estimates of the H I radius to derive $M_{\rm DYN}$, which when compared to $M_{\rm BARY}$ allowed constraints on $M_{\rm DM}$. The typical fraction for our sample is $M_{\rm DM}/M_{\rm DYN} = 62\%$.

We also explored the relationships between $M_{\rm BH}$ and constraints on $M_{\rm DYN}$, $M_{\rm DM}$, and $M_{\rm HALO}$. We found significant correlations between $M_{\rm BH}$–$M_{\rm DYN}$ and $M_{\rm BH}$–$M_{\rm DM}$. To approximate $M_{\rm HALO}$, we assumed $R_{200} \sim (11 \pm 1)$ $R_{\rm HI}$ and a flat rotation curve out to R_{200}. $M_{\rm HALO}$ estimates for this sample showed good agreement with the range of halo masses found by other observationally based methods and simulations (Spitler & Forbes 2009; Bastian et al. 2020). Over the range of $M_{\rm BH}$ and $M_{\rm HALO}$ probed by this sample, we found good agreement between our $M_{\rm BH}$–$M_{\rm HALO}$ relation, the observationally constrained relations of Ferrarese (2002) and Bandara et al. (2009), and the hydrodynamical simulations of Booth & Schaye (2010) and Mutlu-Pakdil et al. (2018).

We thank the referee for helpful suggestions that improved the clarity of this paper. M.C.B gratefully acknowledges support from the NSF through CAREER grant AST-1253702 and grant AST-2009230. H.M.C. acknowledges support by the CNES and Institut Universitaire de France. We thank Mitchell Revalski for advisement of drizzling techniques for archival HST data. We thank Wesley Peters for helpful observing strategies with the APO ARC telescope. We also thank Joanne Hughes for obtaining sky flat observations for the ARCTIC instrument.

This work is based on observations obtained at the MDM Observatory, operated by Dartmouth College, Columbia University, Ohio State University, Ohio University, and the University of Michigan.

This work is based on observations obtained with the Apache Point Observatory 3.5 m telescope, which is owned and operated by the Astrophysical Research Consortium, and with Apache Point Observatory's 0.5 m Astrophysical Research Consortium Small Aperture Telescope.

This research has been supported by RECONS (www.recons.org) members Michele Silverstein, Todd Henry, and Wei-Chun Jao, who provided data as part of the long-term astrometry/photometry program at the CTIO/SMARTS 0.9 m, which is operated as part of the SMARTS Consortium.

This research has made use of the NASA/IPAC Extragalactic Database (NED), which is operated by the Jet Propulsion Laboratory, California Institute of Technology, under contract with the National Aeronautics and Space Administration.

Funding for SDSS-III has been provided by the Alfred P. Sloan Foundation, the Participating Institutions, the National Science Foundation, and the U.S. Department of Energy Office of Science. The SDSS-III website is http://www.sdss3.org/.

Appendix

In Section 5.2, we presented the derivations of the inclination and redshift corrections for the *V*-band TF calibration. Here, we describe those derivations in detail.

To constrain the inclination-dependent correction for the *V*-band TF calibration, we have followed the same procedures described by Tully et al. (1998). Their analysis includes *B*, *R*, *I*, and K' photometric data from two nearby galaxy clusters. The first is the Ursa Major cluster, whose data are available from Tully et al. (1996). The second is the Pisces Cluster, whose data were used in the analysis of Tully et al. (1998), but were not made publicly available until the work of Tully & Pierce (2000). Two tests of extinction as a function of galaxy inclination were conducted by Tully et al. (1998), the first and most sensitive of which describes constructing color–magnitude diagrams of *B*, *R*, and *I* passbands relative to the K' passband. Reddening effects in K' are small, therefore, the extinction effects on the galaxies are dominant in the color terms. We identified all galaxies in both clusters used in the analysis of Tully et al. (1998), and collected available *V*-band magnitudes from RC3, as the adopted *B*-band magnitudes of

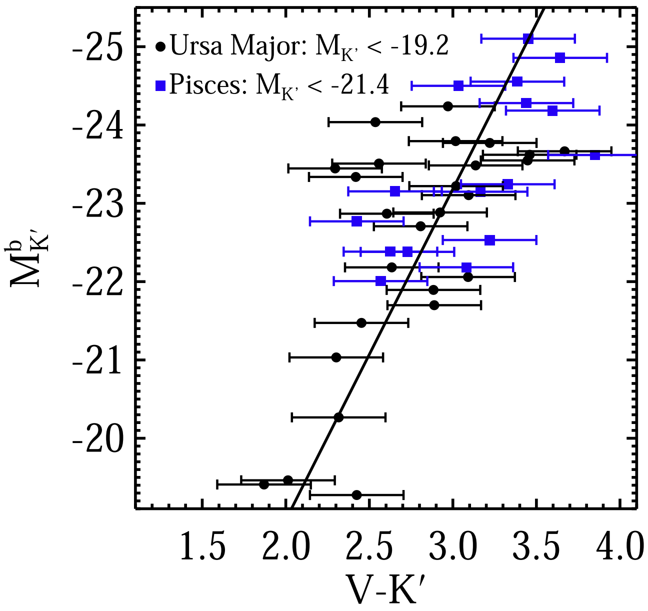

Figure 10. Color–magnitude diagram for the Ursa Major and Pisces clusters used for the analysis of the inclination-dependent extinction correction for our TF *V*-band calibration. Ursa major galaxies are displayed as black circles, Pisces galaxies as blue squares. The Ursa Major cluster data is available in Tully et al. (1996), and the Pisces cluster in Tully & Pierce (2000). The *V*-band magnitudes were retrieved from RC3. The $M_{\mathrm{K}'}$ values were derived using the same distance moduli in the original analysis of Tully et al. (1998), 31.33 for Ursa Major and 33.88 for Pisces. The cuts to $M_{\mathrm{K}'}$ for each cluster are also consistent with their analysis. *V*- and *K*′-band magnitude uncertainties are assumed to be 0.2 mag (see the Appendix). The line is a linear regression with uncertainties in color.

Tully et al. (1998) show an almost exact match to those listed in RC3.

We adopt the same K' apparent magnitudes and distance moduli reported by Tully et al. (1998) for each cluster (31.33 for Ursa Major, 33.88 for Pisces) to derive absolute K' magnitudes. The apparent magnitudes in their analysis include *k*-corrections and Galactic extinction corrections. They detail that the *k*-corrections were extremely small given the proximity of each cluster; specifically, they report *k*-corrections of ∼0 mag for the Ursa Major galaxies and $\sim 0.03 \pm 0.03$ mag for the Pisces galaxies at B, and even less significant ($\lesssim$0.01 mag) in the redder bands. Therefore, we have not considered *k*-corrections for the V band for this portion of our analysis. The Galactic extinction corrections for the B band were drawn from Burstein & Heiles (1984), and Tully et al. (1998) reported extinction ratios between the separate bands, yet did not detail how they arrived at the given ratios. In order to estimate the extinction ratio for the V band, we assumed an average extinction curve of $R = A_V/E(B - V) = 3.1$ (Savage & Mathis (1979), which also approximates the R/B and I/B extinction ratios listed by Tully et al. (1998) to within ∼0.05), and arrived at an extinction ratio of $V/B = 0.76$.

In Figure 10, we display the absolute K' magnitudes versus $V - K'$ color. Ursa Major galaxies are plotted in black circles, Pisces galaxies in blue squares. We make consistent magnitude cuts ($M_{K'} < -19.2$ for Ursa Major, $M_{K'} < -21.4$ for Pisces), which Tully et al. (1998) detail as the cutoffs for their K'-band completeness limits. Several of the lower-luminosity galaxies that were originally included in the Tully et al. (1998) analysis do not have V-band magnitudes available in RC3, so the low-luminosity end of the color–magnitude diagram is only sparsely populated. Tully et al. (1998) describe their linear regression to the color–magnitude diagram with uncertainties in the color, yet no uncertainties are provided for the magnitudes. We find that we can reasonably reproduce the results of Tully et al. (1998). For the B band when a typical uncertainty of 0.2 mag is assumed for the photometry. Thus, we adopt 0.2 mag uncertainty for the V and K' magnitudes, and find a best fit of $M^b_{K'} = (-4.23 \pm 0.56)(V - K') - (10.50 \pm 1.67)$.

The next portion of the analysis assumes that deviations from the mean of the color–magnitude relation (given by the best-fit line in Figure 10) are dominated by inclination-dependent obscuration. Tully et al. (1998) found that the extinction dependence on inclination is also a function of luminosity, where brighter galaxies have a much higher dependence than fainter galaxies. To quantify the luminosity dependencies for the $B - K'$, $R - K'$, and $I - K'$ colors, they separated the galaxies into four luminosity bins and plotted the deviations as a function of disk axis ratio. In Figure 11, we show the deviations from the $V - K'$ fit as a function of axis ratio. Following Tully et al. (1998), we have split the sample into four bins, but with slightly different bin centers that account for the small number of galaxies at the lowest luminosities.

The extinction parameter is often described as $A_i^\lambda = \gamma_\lambda \log(a/b)$, where λ is the passband and a/b is the ratio of major to minor axes. The solid black lines in Figure 11 are the best fits, where the slope is γ and where A_i^V is assumed to be $(V - K') - (V - K')_{\mathrm{fit}}$. We find smaller deviations from the mean color at lower galaxy luminosities, in agreement with the findings of Tully et al. (1998). In the lowest luminosity bin, we find a best fit with a negative slope, which is nonphysical, but is also formally consistent with zero. For that bin, we therefore adopt a slope of 0.00 ± 0.40. In Figure 12 we display the best-fit slope for each bin versus the absolute V-band magnitude associated with the median luminosity of each bin, corrected for inclination and Galactic extinction. We assume a linear function for the magnitude dependence of the inclination-dependent extinction correction, and find $\gamma_V = (-0.39 \pm 0.14)M_V^{b,i} - (6.91 \pm 2.79)$. We find a negligible change if we instead employ the median $M_{K'}$ of each bin and adopt the $(V - K')$ value of the fit in Figure 10 to predict $M_V^{b,i}$. With this method, we find $\gamma_V(-0.36 \pm 0.13)M_V^{b,i} - (6.31 \pm 2.60)$, where the slopes are nearly identical and the intercept has shifted slightly, but is well within the uncertainties.

The last step in the analysis of Tully et al. (1998) involves applying the inclination corrections to the absolute magnitudes in order to re-derive the luminosity–H I line width relation. The definition of the line width parameter used here and in Tully et al. (1998) predates the newer definition of Courtois et al. (2009), so we denote this previous version as W_{R}^i for consistency. We adopt the same line widths and uncertainties from Tully et al. (1998). We apply our derived inclination corrections to the V-band absolute magnitudes of the galaxies in the Pisces and Ursa Major clusters, and plot them against the corresponding W_{R}^i values in Figure 13. The solid line is the best fit, $M_V^{b,i} = (-20.44 \pm 0.01) - (7.57 \pm 0.01)(\log W_{\mathrm{R}}^i - 2.5)$. Lastly, our equations for γ_V and $M_V^{b,i}$ can now be used to derive γ_V solely in terms of the distance-independent variable W_{R}^i, which we find to be $\gamma_V = (1.01 \pm 4.06) + (2.94 \pm 1.09)(\log W_{\mathrm{R}}^i - 2.5)$.

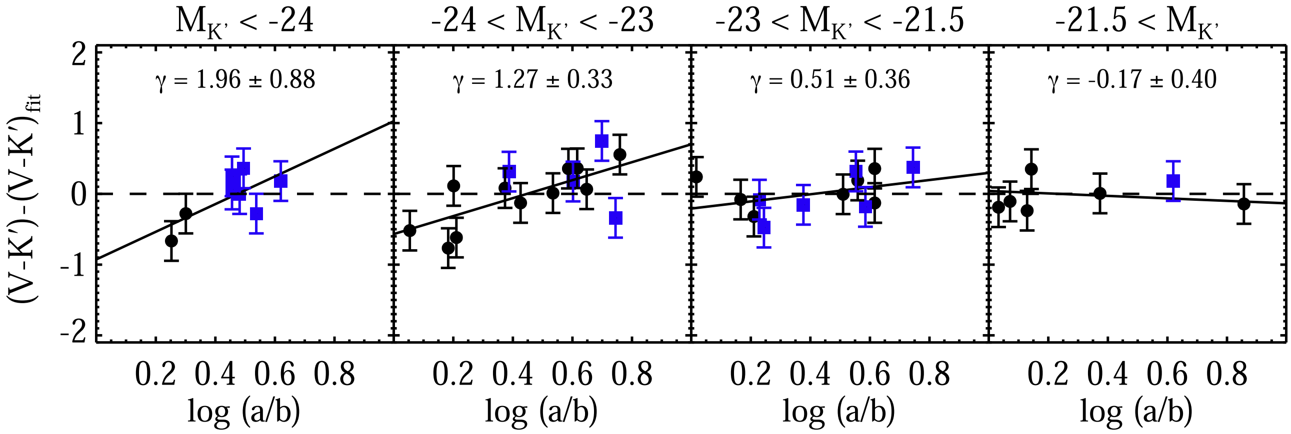

Figure 11. Deviations of $V - K'$ from the mean (best-fit line) of the color–magnitude relation of Figure 10 as a function of the log of the axis ratio of each galaxy. The centers of the four luminosity bins are adjusted from those used by Tully et al. (1998) to better evenly separate the data. Black circles are members of the Ursa Major cluster, and blue squares are members of the Pisces cluster. The solid black lines are linear regression solutions to $A_i^\lambda = \gamma_\lambda \log(a/b)$. The lack of data in the lowest luminosity bin resulted in a nonphysical negative slope, and we adopt 0.00 ± 0.40 for this bin for the remainder of our analysis.

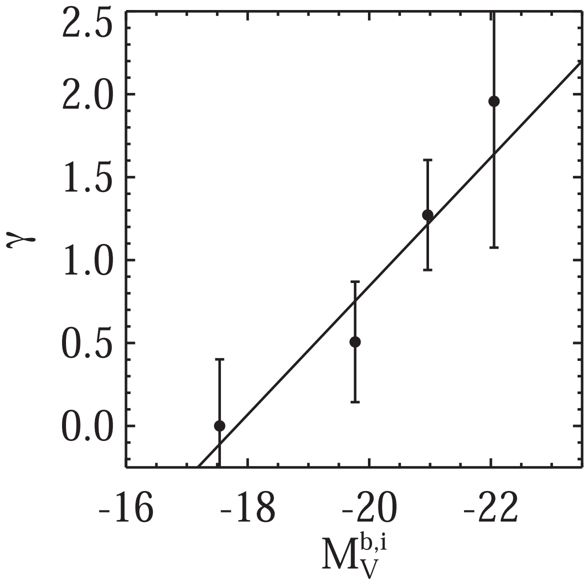

Figure 12. Dependency of the γ values from the fits displayed in Figure 11 of each K' luminosity bin. The four points are the median $M_V^{b,i}$ values of each bin, and were derived from the distance moduli to each cluster used in the original analysis of Tully et al. (1998). The magnitudes were first corrected for galactic extinction and second for inclination-dependent extinction from each corresponding K' luminosity bin. The solid line is a linear regression with uncertainties in γ from the fits in each bin.

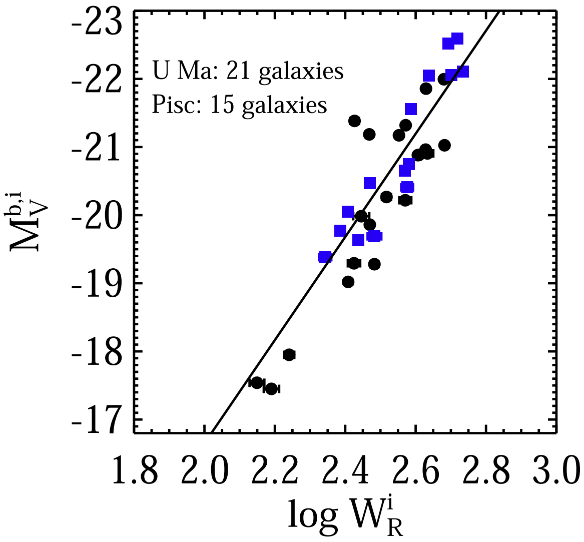

Figure 13. The TF relation of the calibrating sample of Tully et al. (1998) for the V-band inclination-dependent extinction correction. Ursa major galaxies are displayed as black circles, Pisces galaxies as blue squares. The absolute V-band magnitudes are corrected for galactic extinction and inclination-dependent extinction using the best-fit solution for $A_i^\lambda = \gamma_\lambda \log(a/b)$ in Figure 12. The former width parameter W_R is used here. The solid line is the best fit to the data, with uncertainties in the H I line widths from Tully et al. (1998).

With the inclination-dependent extinction correction defined, we next turn to the k-correction. With no reference for their calibrating data set, we have assumed the data used to constrain the prescriptions of Tully & Pierce (2000) may come from the well-cited work of Frei & Gunn (1994). Their study reports k-corrections in the B band (k_B) for various colors for galaxies with Hubble types E, Sbc, Scd, and Sm that are located between $0 < z < 0.6$. When used with their prescription $k_B(z) = B(z) - B(z = 0) - 2.5\log(1 + z)$, the k-correction in any filter can be derived by taking the difference between B and another magnitude, using the corresponding color information they provide. We tested our assumption by comparing the data from Frei & Gunn (1994) to the prescriptions of Tully & Pierce (2000). The results are shown in Figure 14. The left panel contains the k-corrections for the B band, and the right for the R and I bands. The lines in each are best fits to the data, where the B and $R{-}I$ fits are from Tully & Pierce (2000), given as $A_k^B = (3.6 - 0.36T)z$ and $A_k^R = [4.24(R - I) - 1.10]z$, respectively. We found excellent agreement for the B-band data, however, only if we shift each Hubble type T to a lower integer. For example, Hubble type Sbc corresponds to $T = 4$, yet we only find a satisfactory fit to the Sbc k-corrections if $T = 3$ is used. The same is true for Scd, where we find a matching fit if $T = 5$ is used, as opposed to $T = 6$. For the Sm data, which normally corresponds to $T = 9$, we find a good fit if $T = 7$ is used. For the R and I k-corrections, Tully & Pierce (2000) prescribe one fit to characterize both sets of data. We find good agreement with the

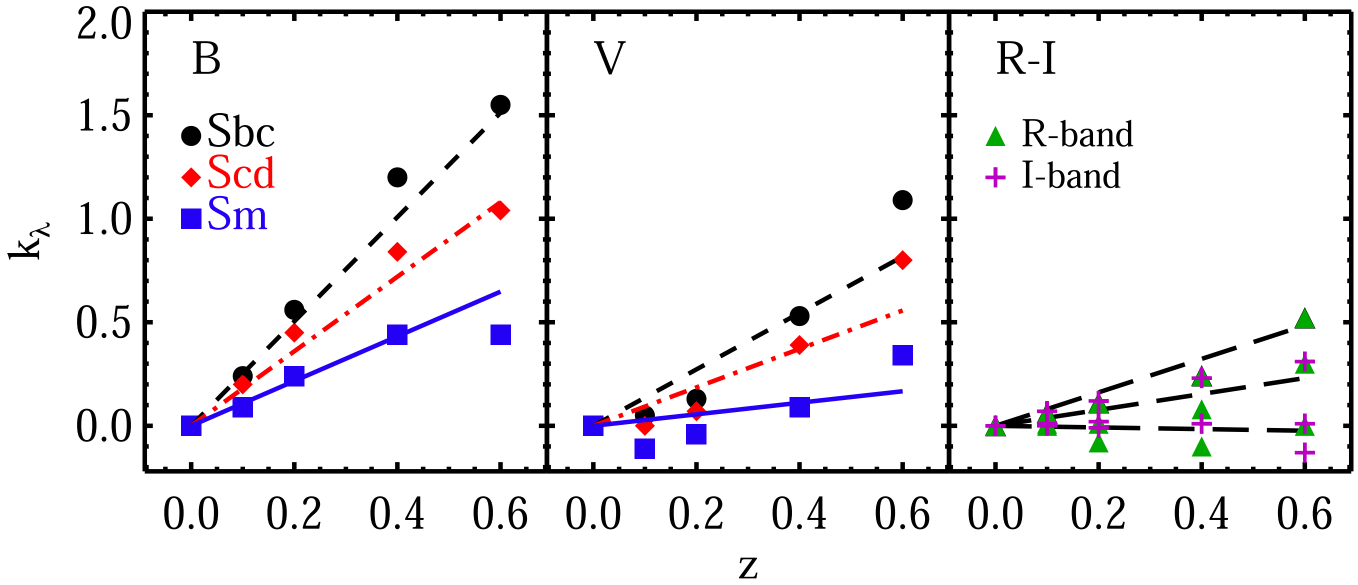

Figure 14. *k*-corrections for the *B*, *V*, *R*, and *I* bands. Data were retrieved from Frei & Gunn (1994). The black (dashed), red (dotted–dashed), and blue (solid) lines in the left panel, and the black double dashed lines in the right panel, are the *B* and *R*−*I* *k*-correction prescriptions from Tully & Pierce (2000), respectively. Excellent agreement is found when Hubble type Sbc corresponds to $T = 3$, Scd to $T = 5$, and Sm to $T = 7$. The fits in the right panel assume $R - I$ values of 0.45, 0.35, and 0.25 for the top, middle, and bottom lines. The middle panel displays our best fits to the *V*-band *k*-corrections (where Sbc, Scd, and Sm correspond to *T* values of 4, 6, and 9, respectively), constrained such that $k_V = 0$ at $z = 0$.

data from Frei & Gunn (1994) when *R*−*I* values of 0.45, 0.35, and 0.25 are adopted for Sbc, Scd, and Sm types.

Given that our assumption of Tully et al. (1998) basing their work on the data of Frei & Gunn (1994) seems to hold, we therefore determined the *k*-correction in a similar way for the *V* band, and display it in the center panel of Figure 14. The corrections in the *B* band are highly dependent on the morphological classification, while the *R* and *I* bands have much less of a spread as a function of morphology. This is reflected in the formalisms of each correction, as *T* is a factor in the *B*-band calibration yet is absent in the $R - I$ calibration. While the *V* band has less of a dependence on morphology than the *B* band, we nevertheless sought to arrive at a morphologically-dependent calibration given the obvious spread as a function of *T*. We assume, as we did with the *B* band, that the Sbc, Scd, and Sm classifications correspond to $T = 4$, 6, and 9, respectively, and that $k_V = 0$ at $z = 0$. We fit the data for the three Hubble types, and solved for a universal fit such that *T* was a scale factor which yielded the three solutions, and arrived at $A_k^V = (2.23 - 0.22T)z$.

While the *k*-corrections are derived using galaxies out to $z = 0.6$, the TF method is only applicable to galaxies at $z \lesssim 0.1$ (Reyes et al. 2011), and Tully & Pierce (2000) describe the corrections as always <0.08 mag in the *B* band. The maximum expected *k*-correction in the *V* band is 0.2, which would correspond to $T = 1$ at $z = 0.1$. This correction is larger than the upper limit reported by Tully & Pierce (2000) for the *B* band, however, $z \lesssim 0.03$ for their sample.

Finally, with the inclination and *k*-corrections in hand, we were able to derive the *V*-band TF relation. We first identified all galaxies in the calibrating sample of Tully et al. (2008) that had distances derived from Cepheids, TRGB, and SBF. From their VizieR table, we retrieved the *B*-band magnitudes, distance moduli, and $W_{\rm R}^i$ values. In addition, we retrieved all available *B*- and *V*-band magnitudes from RC3, as well as all original distance moduli and uncertainties from the literature for the calibrating sample. The distances reported by Tully et al. (2008) match the original published values and do not appear to have been updated in any way.

We first aimed to recreate the fit to the *B*-band relationship by Tully et al. (2008). Since the difference was negligible, we began by using the originally published values of the distance moduli and uncertainties, with *B*-band magnitudes from RC3. Galactic extinction values were retrieved from Schlegel et al. (1998), and inclination and *k*-corrections were applied with Equations (11) and (14). The difference in fits using *B*-band apparent magnitudes from RC3 versus magnitudes from Tully et al. (2008) was negligible. When the published uncertainties on the distance measurements were used to convert apparent magnitudes to absolute magnitudes, the fit resulted in a slightly steeper slope than that reported, as shown in the top panel of Figure 15, where the reported fit from Tully et al. (2008) is the red dashed line, and our best fit is the blue dotted–dashed line. Tully et al. (2008) asserted that galaxies with distances from Cepheids, TRGB, or SBF are assumed to have a 0.2 mag uncertainty in their moduli. If we adopt this, we reproduce the *B*-band fit almost exactly, shown as the solid black line in Figure 15.

Thus, the *V*-band apparent magnitudes from RC3 for the calibrating sample of Tully et al. (2008) were corrected for Galactic extinction using values from Schlegel et al. (1998), and for inclination-dependent extinction and *k*-corrections using Equations (17) and 18. The distance moduli were then used to convert the corrected apparent magnitudes to absolute magnitudes, with 0.2 mag typical uncertainty adopted for the distance moduli. Our best fit to the relationship between $M_V^{b,i,k}$ and $W_{\rm R}^i$ for the calibrating sample is shown in the bottom panel of Figure 15, and is given by Equation (19) as $M_V^{b,i,k} = (-20.39 \pm 0.03) - (7.62 \pm 0.15)(\log W_{\rm mx}^i - 2.5)$.

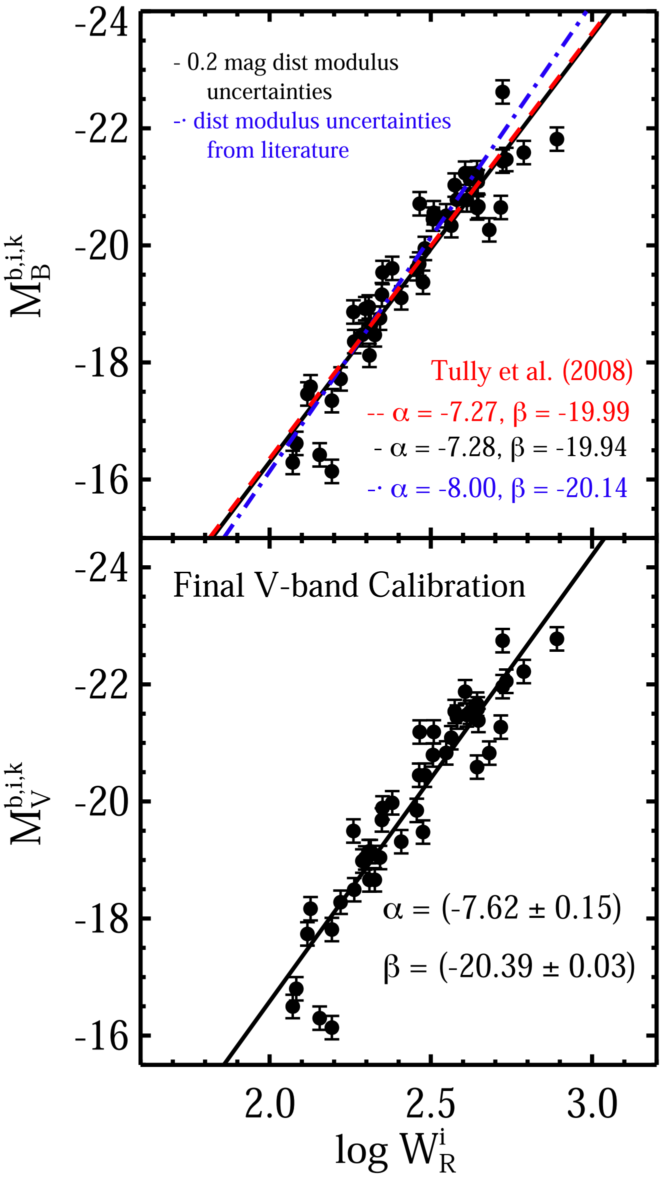

Figure 15. TF *B*-band calibration (top) and our final TF *V*-band calibration (bottom). *B*-band magnitudes, widths, and distance moduli were retrieved from Tully et al. (2008) for galaxies that had primary distance measurements from either Cepheids, TRGB, and/or SBF. *V*-band magnitudes were retrieved from RC3. The red dashed line in the top panel is the fit reported by Tully et al. (2008). The blue dotted–dashed line is our fit using published distance modulus uncertainties, which resulted in a steeper slope than that reported (the slopes and intercepts of which are displayed; the top is the fit given by Tully et al. 2008, the bottom corresponds to the blue dotted–dashed fit). Adopting 0.2 mag uncertainty in the moduli achieves a near perfect match to the fit by Tully et al. (2008), shown as the solid black line and displayed as the middle slope and intercept. The solid black line in the bottom panel is our best fit to the *V*-band TF calibration using distance moduli with 0.2 mag uncertainties, Galactic extinction corrections from Schlegel et al. (1998), and our calibrations for the *V*-band inclination correction (see Equation (17), Figure 13) and *k*-correction (see Equation (18), Figure 14.)

ORCID iDs

Justin H. Robinson https://orcid.org/0000-0002-4262-4845
Misty C. Bentz https://orcid.org/0000-0002-2816-5398
Hélène M. Courtois https://orcid.org/0000-0003-0509-1776
Megan C. Johnson https://orcid.org/0000-0002-4146-1618
D. M. Crenshaw https://orcid.org/0000-0002-6465-3639
Beena Meena https://orcid.org/0000-0001-8658-2723
Garrett E. Polack https://orcid.org/0000-0001-5862-2150
Dading Chen https://orcid.org/0000-0001-9276-4339

References

Aaronson, M., Mould, J., Huchra, J., et al. 1980, ApJ, 239, 12
Adams, E. A. K., & van Leeuwen, J. 2019, NatAs, 3, 188
Ahumada, R., Allende Prieto, C., Almeida, A., et al. 2020, ApJS, 249, 3
Bandara, K., Crampton, D., & Simard, L. 2009, ApJ, 704, 1135
Barth, A. J., Bennert, V. N., Canalizo, G., et al. 2015, ApJS, 217, 26
Barth, A. J., Pancoast, A., Bennert, V. N., et al. 2013, ApJ, 769, 128
Barton, E. J., Geller, M. J., Bromley, B. C., van Zee, L., & Kenyon, S. J. 2001, AJ, 121, 625
Bastian, N., Pfeffer, J., Kruijssen, J. M. D., et al. 2020, MNRAS, 498, 1050
Bell, E. F., & de Jong, R. S. 2001, ApJ, 550, 212
Bennett, C. L., Larson, D., Weiland, J. L., & Hinshaw, G. 2014, ApJ, 794, 135
Bentz, M. C., Denney, K. D., Grier, C. J., et al. 2013, ApJ, 767, 149
Bentz, M. C., Ferrarese, L., Onken, C. A., Peterson, B. M., & Valluri, M. 2019, ApJ, 885, 161
Bentz, M. C., & Katz, S. 2015, PASP, 127, 67
Bentz, M. C., & Manne-Nicholas, E. 2018, ApJ, 864, 146
Bentz, M. C., Peterson, B. M., Netzer, H., Pogge, R. W., & Vestergaard, M. 2009a, ApJ, 697, 160
Bentz, M. C., Walsh, J. L., Barth, A. J., et al. 2009b, ApJ, 705, 199
Bernardi, M., Shankar, F., Hyde, J. B., et al. 2010, MNRAS, 404, 2087
Bigiel, F., Leroy, A., Walter, F., et al. 2008, AJ, 136, 2846
Blakeslee, J. P., Cantiello, M., Mei, S., et al. 2010, ApJ, 724, 657
Blandford, R. D., & McKee, C. F. 1982, ApJ, 255, 419
Bolton, A. S., Burles, S., Koopmans, L. V. E., et al. 2008, ApJ, 682, 964
Booth, C. M., & Schaye, J. 2010, MNRAS, 405, L1
Bottinelli, L., Gouguenheim, L., Paturel, G., & de Vaucouleurs, G. 1983, A&A, 118, 4
Bottinelli, L., Gouguenheim, L., Paturel, G., & de Vaucouleurs, G. 1984, A&AS, 56, 381
Bottinelli, L., Gouguenheim, L., Paturel, G., & de Vaucouleurs, G. 1985, A&AS, 59, 43
Bower, R. G., Benson, A. J., Malbon, R., et al. 2006, MNRAS, 370, 645
Broeils, A. H., & Rhee, M. H. 1997, A&A, 324, 877
Bullock, J. S., Kolatt, T. S., Sigad, Y., et al. 2001, MNRAS, 321, 559
Burkert, A. 1995, ApJL, 447, L25
Burstein, D., & Heiles, C. 1984, ApJS, 54, 33
Catinella, B., & Cortese, L. 2015, MNRAS, 446, 3526
Catinella, B., Giovanelli, R., & Haynes, M. P. 2006, ApJ, 640, 751
Chabrier, G. 2003, PASP, 115, 763
Chilingarian, I. V., Melchior, A.-L., & Zolotukhin, I. Y. 2010, MNRAS, 405, 1409
Ciotti, L., Ostriker, J. P., & Proga, D. 2009, ApJ, 699, 89
Courtois, H. M., Tully, R. B., Fisher, J. R., et al. 2009, AJ, 138, 1938
Courtois, H. M., Zaritsky, D., Sorce, J. G., & Pomarède, D. 2015, MNRAS, 448, 1767
Covey, K. R., Ivezić, Ž., Schlegel, D., et al. 2007, AJ, 134, 2398
de Blok, W. J. G., & Walter, F. 2014, AJ, 147, 96
de Blok, W. J. G., Walter, F., Brinks, E., et al. 2008, AJ, 136, 2648
de Vaucouleurs, G. 1948, AnAp, 11, 247
de Vaucouleurs, G., de Vaucouleurs, A., Corwin, H. G., Jr., et al. 1991, S&T, 82, 621
de Vaucouleurs, G., de Vaucouleurs, A., Corwin, J. R., et al. 1976, Second Reference Catalogue of Bright Galaxies, Vol 1976 (Austin, TX: Univ. Texas Press)
de Vaucouleurs, G., Peters, W. L., Bottinelli, L., Gouguenheim, L., & Paturel, G. 1981, ApJ, 248, 408
Djorgovski, S., & Davis, M. 1987, ApJ, 313, 59
Doroshenko, V. T., Sergeev, S. G., Merkulova, N. I., et al. 2006, yCat 0160, J/other/Ap/48
Dressler, A., Lynden-Bell, D., Burstein, D., et al. 1987, ApJ, 313, 42
Du, P., Lu, K.-X., Zhang, Z.-X., et al. 2016, yCat, J/ApJ/825/126
Epstein, E. E. 1964, AJ, 69, 490
Faber, S. M., & Jackson, R. E. 1976, ApJ, 204, 668
Fanidakis, N., Baugh, C. M., Benson, A. J., et al. 2011, MNRAS, 410, 53
Fausnaugh, M. M., Grier, C. J., Bentz, M. C., et al. 2017, ApJ, 840, 97
Fernández, Ximena, Gim, Hansung B., Gorkom, J. H. van, et al. 2016, ApJL, 824, L1
Ferrarese, L. 2002, ApJ, 578, 90
Ferrarese, L., & Merritt, D. 2000, ApJL, 539, L9
Frei, Z., & Gunn, J. E. 1994, AJ, 108, 1476
Ganeshalingam, M., Li, W., & Filippenko, A. V. 2013, MNRAS, 433, 2240

Gebhardt, K., Bender, R., Bower, G., et al. 2000, ApJL, 539, L13
Gültekin, K., Richstone, D. O., Gebhardt, K., et al. 2009, ApJ, 698, 198
Graves, G. J., & Faber, S. M. 2010, ApJ, 717, 803
Graziani, R., Courtois, H. M., Lavaux, G., et al. 2019, MNRAS, 488, 5438
Grier, C. J., Martini, P., Watson, L. C., et al. 2013, ApJ, 773, 90
Heckman, T. M., & Best, P. N. 2014, ARA&A, 52, 589
Henden, A., & Munari, U. 2014, CoSka, 43, 518
Henden, A. A., Templeton, M., Terrell, D., et al. 2016, yCat, 2336, 0
Ho, L. C., Darling, J., & Greene, J. E. 2008, ApJS, 177, 103
Hoekstra, H., Hsieh, B. C., Yee, H. K. C., Lin, H., & Gladders, M. D. 2005, ApJ, 635, 73
Holmberg, E. 1958, MeLuS, 136, 1
Hu, C., Du, P., Lu, K.-X., et al. 2015, ApJ, 804, 138
Ianjamasimanana, R., de Blok, W. J. G., Walter, F., & Heald, G. H. 2012, AJ, 144, 96
Iben, I., Jr., & Renzini, A. 1983, ARA&A, 21, 271
Iorio, G., Fraternali, F., Nipoti, C., et al. 2017, MNRAS, 466, 4159
Jaffé, Y. L., Poggianti, B. M., Verheijen, M. A. W., Deshev, B. Z., & van Gorkom, J. H. 2013, MNRAS, 431, 2111
Jiang, L., Fan, X., Vestergaard, M., et al. 2007, AJ, 134, 1150
Kaspi, S., Smith, P. S., Netzer, H., et al. 2000, ApJ, 533, 631
Kelly, B. C. 2007, ApJ, 665, 1489
Klypin, A. A., Trujillo-Gomez, S., & Primack, J. 2011, ApJ, 740, 102
Koratkar, A. P., & Gaskell, C. M. 1991, ApJL, 370, L61
Koribalski, B. S., Wang, J., Kamphuis, P., et al. 2018, MNRAS, 478, 1611
Koribalski, B. S., Staveley-Smith, L., Westmeier, T., et al. 2020, Ap&SS, 365, 118
Kormendy, J., & Ho, L. C. 2013, ARA&A, 51, 511
Kormendy, J., & Richstone, D. 1995, ARA&A, 33, 581
Koshida, S., Yoshii, Y., Kobayashi, Y., et al. 2017, ApJL, 842, L13
Kourkchi, E., Tully, R. B., Anand, G. S., et al. 2020, ApJ, 896, 3
Kravtsov, A. V. 2013, ApJ, 764, L31
Kurk, J. D., Walter, F., Fan, X., et al. 2009, ApJ, 702, 833
Kurk, J. D., Walter, F., Fan, X., et al. 2007, ApJ, 669, 32
Kurucz, R. L. 1993, yCat, 6039, 0
Lapi, A., Salucci, P., & Danese, L. 2018, ApJ, 859, 2
Leavitt, H. S., & Pickering, E. C. 1912, HarCi, 173, 1
Lelli, F., McGaugh, S. S., & Schombert, J. M. 2015, ApJ, 816, L14
Lelli, F., McGaugh, S. S., Schombert, J. M., Desmond, H., & Katz, H. 2019, MNRAS, 484, 3267
Leroy, A. K., Walter, F., Brinks, E., et al. 2008, AJ, 136, 2782
Lovell, M. R., Pillepich, A., Genel, S., et al. 2018, MNRAS, 481, 1950
Maddox, N., Frank, B. S., Ponomareva, A. A., et al. 2021, A&A, 646, A35
Mancera Piña, P. E., Fraternali, F., Adams, E. A. K., et al. 2019, ApJL, 883, L33
Mandelbaum, R., Seljak, U., Kauffmann, G., Hirata, C. M., & Brinkmann, J. 2006, MNRAS, 368, 715
Marganian, P., Garwood, R. W., Braatz, J. A., Radziwill, N. M., & Maddalena, R. J. 2006, in ASP Conf. Ser., 351, Astronomical Data Analysis Software and Systems XV, ed. C. Gabriel et al. (San Francisco, CA: ASP), 512
Martin, C. L., & Kennicutt, R. C., Jr. 2001, ApJ, 555, 301
McGaugh, S. S. 2005, ApJ, 632, 859
McGaugh, S. S. 2012, AJ, 143, 40
McGaugh, S. S., Schombert, J. M., Bothun, G. D., & de Blok, W. J. G. 2000, ApJL, 533, L99
Mirabel, I. F., & Sanders, D. B. 1988, ApJ, 335, 104
Mirabel, I. F., & Wilson, A. S. 1984, ApJ, 277, 92
Misgeld, I., & Hilker, M. 2011, MNRAS, 414, 3699
Mould, J. 2020, FrASS, 7, 21
Mundell, C., Pedlar, A. G., Axon, D. J., Meaburn, J., & Unger, S. W. 1995, MNRAS, 277, 641
Mundell, C. G., Pedlar, A., Shone, D. L., & Robinson, A. 1999, MNRAS, 304, 481
Mutlu-Pakdil, B., Seigar, M. S., Hewitt, I. B., et al. 2018, MNRAS, 474, 2594
Ott, J., Stilp, A. M., Warren, S. R., et al. 2012, AJ, 144, 123
Papastergis, E., Cattaneo, A., Huang, S., Giovanelli, R., & Haynes, M. P. 2012, ApJ, 759, 138
Peng, C. Y., Ho, L. C., Impey, C. D., & Rix, H.-W. 2002, AJ, 124, 266
Peng, C. Y., Ho, L. C., Impey, C. D., & Rix, H.-W. 2010, AJ, 139, 2097
Persic, M., & Salucci, P. 1995, ApJS, 99, 501
Persic, M., Salucci, P., & Stel, F. 1996, MNRAS, 281, 27
Peterson, B. M. 1993, PASP, 105, 247
Pillepich, A., Vogelsberger, M., Deason, A., et al. 2014, MNRAS, 444, 237
Planck Collaboration, Aghanim, N., Akrami, Y., et al. 2020, A&A, 641, A6
Reyes, R., Mandelbaum, R., Gunn, J. E., Pizagno, J., & Lackner, C. N. 2011, MNRAS, 417, 2347
Riess, A. G., Casertano, S., Yuan, W., Macri, L. M., & Scolnic, D. 2019, ApJ, 876, 85
Riess, A. G., Macri, L. M., Hoffmann, S. L., et al. 2016, ApJ, 826, 56
Roberts, M. S. 1969, AJ, 74, 859
Robinson, J. H., Bentz, M. C., Johnson, M. C., Courtois, H. M., & Ou-Yang, B. 2019, ApJ, 880, 68
Sakai, S., Mould, J. R., Hughes, S. M. G., et al. 2000, ApJ, 529, 698
Salaris, M., & Cassisi, S. 1997, MNRAS, 289, 406
Savage, B. D., & Mathis, J. S. 1979, ARA&A, 17, 73
Schaye, J. 2004, ApJ, 609, 667
Schlafly, E. F., & Finkbeiner, D. P. 2011, ApJ, 737, 103
Schlegel, D. J., Finkbeiner, D. P., & Davis, M. 1998, ApJ, 500, 525
Sersic, J. L. 1968, Atlas de Galaxias Australes (Cordoba, Argentina: Observatorio Astronomico)
Shaya, E. J., Tully, R. B., Hoffman, Y., & Pomarède, D. 2017, ApJ, 850, 207
Sheth, K., Regan, M., Hinz, J. L., et al. 2010, PASP, 122, 1397
Silk, J., & Rees, M. J. 1998, A&A, 331, L1
Sorce, J. G., Tully, R. B., Courtois, H. M., et al. 2014, MNRAS, 444, 527
Spitler, L. R., & Forbes, D. A. 2009, MNRAS, 392, L1
Steinborn, L. K., Dolag, K., Hirschmann, M., Prieto, M. A., & Remus, R.-S. 2015, MNRAS, 448, 1504
Tamburro, D., Rix, H.-W., Leroy, A. K., et al. 2009, AJ, 137, 4424
Theureau, G., Hanski, M. O., Coudreau, N., Hallet, N., & Martin, J. M. 2007, A&A, 465, 71
Tinker, J., Kravtsov, A. V., Klypin, A., et al. 2008, ApJ, 688, 709
Tonry, J. L., Dressler, A., Blakeslee, J. P., et al. 2001, ApJ, 546, 681
Trujillo, I., Chamba, N., & Knapen, J. H. 2020, MNRAS, 493, 87
Tsvetkov, D. Y., Baklanov, P. V., Potashov, M. S., et al. 2019, MNRAS, 487, 3001
Tully, R. B., & Courtois, H. M. 2012, ApJ, 749, 78
Tully, R. B., Courtois, H. M., & Sorce, J. G. 2016, AJ, 152, 50
Tully, R. B., & Fisher, J. R. 1977, A&A, 54, 661
Tully, R. B., & Fisher, J. R. 1988, Catalog of Nearby Galaxies (Cambridge: Cambridge Univ. Press)
Tully, R. B., & Fouque, P. 1985, ApJS, 58, 67
Tully, R. B., & Pierce, M. J. 2000, ApJ, 533, 744
Tully, R. B., Pierce, M. J., Huang, J.-S., et al. 1998, AJ, 115, 2264
Tully, R. B., Rizzi, L., Shaya, E. J., et al. 2009, AJ, 138, 323
Tully, R. B., Shaya, E. J., Karachentsev, I. D., et al. 2008, ApJ, 676, 184
Tully, R. B., Verheijen, M. A. W., Pierce, M. J., Huang, J.-S., & Wainscoat, R. J. 1996, AJ, 112, 2471
Tully, R. B., Courtois, H. M., Dolphin, A. E., et al. 2013, AJ, 146, 86
Veilleux, S., Kim, D.-C., Rupke, D. S. N., et al. 2009, ApJ, 701, 587
Vestergaard, M., & Peterson, B. M. 2006, ApJ, 641, 689
Volonteri, M., Dubois, Y., Pichon, C., & Devriendt, J. 2016, MNRAS, 460, 2979
Walter, F., Brinks, E., de Blok, W. J. G., et al. 2008, AJ, 136, 2563
Wang, J., Koribalski, B. S., Serra, P., et al. 2016, MNRAS, 460, 2143
Wang, J.-M., Du, P., Hu, C., et al. 2014, ApJ, 793, 108
Willott, C. J., Albert, L., Arzoumanian, D., et al. 2010, AJ, 140, 546
Wong, T., & Blitz, L. 2002, ApJ, 569, 157
Xue, Y. Q., Brandt, W. N., Luo, B., et al. 2010, ApJ, 720, 368
Yegorova, I., Babic, A., Salucci, P., Spekkens, K., & Pizzella, A. 2011, AN, 332, 846
Yuan, W., Fausnaugh, M. M., Hoffmann, S. L., et al. 2020b, ApJ, 902, 26
Yuan, W., Macri, L. M., Peterson, B. M., et al. 2020a, arXiv:2012.05931
Zaritsky, D., Courtois, H., Muñoz-Mateos, J.-C., et al. 2014, AJ, 147, 134
Zhang, H.-X., Hunter, D. A., Elmegreen, B. G., Gao, Y., & Schruba, A. 2012, AJ, 143, 47